POLITECNICO DI TORINO

Master of Science in Mechanical Engineering

· Mechanical Design ·

Master’s Thesis

Development and LCD 3D printing of a vitrimer based on glycerol 1,3-diglycerolate diacrylate and acrylated epoxidized soybean oil

Supervisors

Camilla Noè
Massimo Messori

Candidate

Antonio Iaia

April 2026

Table of contents

List of figures

List of tables

Abstract

In the field of additive manufacturing, conventional thermosetting resins are widely valued for their excellent mechanical and thermal properties. However, their permanent cross-linked structure precludes reprocessability, repair, and recycling, thereby fueling environmental concerns regarding the accumulation of persistent plastic waste. Within this scenario, vitrimers emerge as a promising alternative: by leveraging dynamic covalent networks, that allow for topological rearrangement under specific stimuli, these innovative polymers successfully combine the structural integrity of thermosets with the reprocessability of thermoplastics.

Aiming to integrate environmental sustainability with advanced functional performance, the present study focused on the development and comprehensive characterization of a novel bio-based photopolymerizable vitrimer resin, specifically designed for high-resolution LCD 3D printing. The system, based on glycerol 1,3-diglycerolate diacrylate (GDGDA) and acrylated epoxidized soybean oil (AESO), was analyzed by evaluating the impact of the monomeric balance and the transesterification catalysis on both process kinetics and printed materials' final properties.

A wide range of characterization techniques was employed to investigate the chemical, rheological, thermal, and mechanical properties, as well as the network rearrangement of the developed vitrimer systems.

Viscosity analysis and photorheology facilitated the definition of resins' printability and the monitoring of viscoelastic properties evolution during UV curing, while FTIR spectroscopy was utilized to analyze the chemical structure and quantify the degree of conversion of reactive functional groups post-polymerization. In parallel, the application of Jacob's working equation proved fundamental for optimizing key printing parameters, such as exposure time and layer thickness, to ensure accurate layer-by-layer fabrication.

Thermal properties of the printed specimens were analyzed via *differential scanning calorimetry* (DSC), providing insights into the glass transition range and the degree of polymerization. These findings were complemented by *dynamic-mechanical thermal analysis* (DMTA), which allowed for a detailed evaluation of viscoelastic and thermo-mechanical behavior, alongside a more precise measurement of glass transition temperatures.

The dynamic nature of the vitrimer network was examined through stress-relaxation tests performed at elevated temperatures, enabling the study of bond-exchange kinetics and the calculation of the activation energy associated with transesterification reactions.

Mechanical performance was assessed via standardized tensile and impact tests, allowing for the evaluation of stiffness, strength, ductility, and toughness of the 3D-printed samples. In addition, the characteristic functional properties of vitrimer systems were explored through dedicated experiments, including thermally induced self-healing of surface damage, and reprocessing tests via thermal welding of fractured specimens under pressure.

Overall, this study provides a comprehensive framework for the design, processing, and characterization of sustainable vitrimer resins for additive manufacturing. The investigated formulations demonstrated excellent printability and compatibility with LCD technology, enabling the fabrication of high-resolution complex structures. Furthermore, the materials exhibited effective dynamic behavior, characterized by significant stress-relaxation capabilities and thermally activated self-healing properties. By integrating bio-based chemistry and dynamic covalent network design with 3D printing, this research offers a concrete model for the development of next-generation polymeric materials aligned with circular economy principles.

Sommario

Nel campo della manifattura additiva, le resine termoindurenti convenzionali sono largamente apprezzate per le eccellenti proprietà meccaniche e termiche. Tuttavia, la loro struttura reticolare permanente ne impedisce la riprocessabilità, la riparazione e il riciclo, alimentando le preoccupazioni ambientali legate all'accumulo di rifiuti plastici permanenti. In questo scenario, i vitrimeri emergono come un'alternativa promettente: grazie a reti covalenti dinamiche, che consentono il riarrangiamento topologico sotto specifici stimoli, questi polimeri innovativi riescono a coniugare l'integrità strutturale dei termoindurenti con la riprocessabilità tipica dei termoplastici.

Con l'obiettivo di unire sostenibilità ambientale e prestazioni funzionali avanzate, il presente studio si è focalizzato sullo sviluppo e sulla caratterizzazione approfondita di una nuova resina vitrimerica fotopolimerizzabile a base biologica, specificamente progettata per la stampa 3D LCD ad alta risoluzione. Il sistema, basato su *glicerolo 1,3-diglicerolato diacrilato* (GDGDA) e *olio di soia epossidato acrilato* (AESO), è stato quindi analizzato valutando l'impatto del bilancio monomerico e della catalisi di transesterificazione sulla cinetica di processo e sulle proprietà finali dei materiali stampati.

È stata impiegata un'ampia gamma di tecniche di caratterizzazione per studiare le proprietà chimiche, reologiche, termiche, meccaniche ed il riarrangiamento del network dei sistemi vitrimerici sviluppati.

L'analisi di viscosità e la fotoreologia hanno permesso di definire la stampabilità delle resine e di monitorare l'evoluzione delle proprietà viscoelastiche durante la cura UV, mentre la spettroscopia FTIR è stata impiegata per analizzare la struttura chimica dei materiali e quantificare il grado di conversione dei gruppi funzionali reattivi dopo la polimerizzazione. Parallelamente, l'applicazione dell'equazione di Jacob è stata fondamentale per ottimizzare i parametri di stampa (tempo di esposizione e altezza del layer) e garantire una corretta fabbricazione strato su strato.

Le proprietà termiche dei materiali stampati sono state analizzate mediante *calorimetria differenziale a scansione* (DSC), che ha fornito informazioni sull'intervallo di transizione vetrosa e sul grado di polimerizzazione. Questo test è stato integrato dall'*analisi dinamico-meccanica termica* (DMTA), che ha permesso una valutazione dettagliata del comportamento

viscoelastico e termo-meccanico, oltre a fornire una misurazione più accurata delle temperature di transizione vetrosa.

La natura dinamica della rete vitrimerica, invece, è stata analizzata attraverso prove di *stress-relaxation* condotte ad alte temperature, che hanno consentito di studiare la cinetica dei processi di scambio dei legami e di calcolare l'energia di attivazione associata alle reazioni di transesterificazione.

Le prestazioni meccaniche sono state valutate attraverso prove standardizzate di trazione e impatto, che hanno permesso di determinare rigidezza, resistenza, duttilità e tenacità dei campioni stampati in 3D. Inoltre, sono state esplorate le proprietà funzionali tipiche dei vitrimeri mediante esperimenti dedicati, tra cui prove di autoriparazione (*self-healing*), basate sul ripristino, indotto termicamente, di danneggiamenti superficiali, e test di riprocessabilità, tramite saldatura termica sotto pressione di campioni fratturati.

Nel complesso, questo studio fornisce un quadro completo per la progettazione, il processamento e la caratterizzazione di resine vitrimeriche sostenibili per applicazioni di manifattura additiva. Le formulazioni studiate hanno mostrato un'eccellente stampabilità e compatibilità con la tecnologia LCD, consentendo la realizzazione di strutture complesse ad alta risoluzione. Inoltre, i materiali hanno evidenziato un comportamento dinamico efficace, caratterizzato da una significativa capacità di rilassamento degli sforzi e da proprietà di autoriparazione attivabili termicamente. Integrando la chimica *bio-based* e la progettazione di reti covalenti dinamiche con la stampa 3D, questa ricerca offre un modello concreto per lo sviluppo di materiali polimerici di nuova generazione, in linea con i principi dell'economia circolare.

1. Introduction and research motivation

The rapid evolution of additive manufacturing has captivated the scientific community due to its unparalleled capacity to transform digital designs into complex physical components through a layer-by-layer deposition process. This technological shift offers significant industrial advantages, particularly in producing intricate geometries that remain unattainable with traditional subtractive methods, while simultaneously enhancing cost-efficiency and minimizing material waste through high-precision customization.

Within this framework, polymeric materials have become indispensable across a wide range of sectors: from automotive and aerospace to the medical field. However, the widespread reliance on conventional thermosetting resins for additive manufacturing presents a critical sustainability challenge. These materials, whose life cycle is schematized in Figure 1**,** are predominantly synthesized from finite fossil fuel resources and are characterized by permanent, irreversible molecular networks that, while providing robust mechanical properties, prevent these materials from being reshaped, healed, or recycled once cured. This inherent lack of reprocessability, coupled with their high resistance to natural degradation, exacerbates the global crisis of plastic accumulation in terrestrial and aquatic environments.

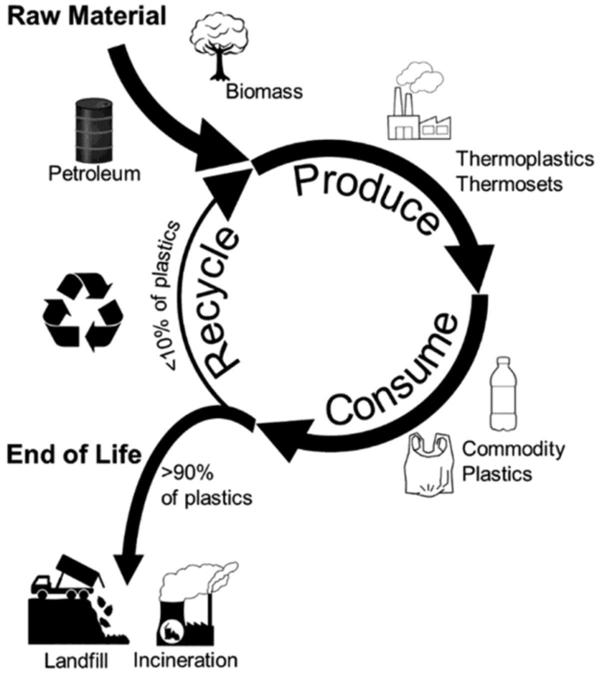

FIGURE 1 - CONVENTIONAL RECYCLING EFFORTS [16]

Consequently, there is a pressing demand, in both academia and industry, to transition toward renewable, bio-based alternatives that align with circular economy principles (Figure 2). In this context, a promising solution lies in the development of vitrimers, an emerging class of polymers equipped with dynamic covalent networks. These structures, when triggered by specific stimuli, undergo controlled bond exchange reactions, enabling advanced functional properties such as self-healing capability, shape-memory behavior, recyclability, and reprocessability.

Building upon these advancements, the primary focus of this research was the development and comprehensive characterization of a sustainable, photocurable vitrimer resin tailored for additive manufacturing via high-resolution LCD 3D printing. The innovation of this work centers on the utilization of a fully bio-derived monomer system, specifically integrating *glycerol 1,3-diglycerolate diacrylate* (GDGDA) and *acrylated epoxidized soybean oil* (AESO) to create a new material that harmonizes advanced functional properties with environmental responsibility.

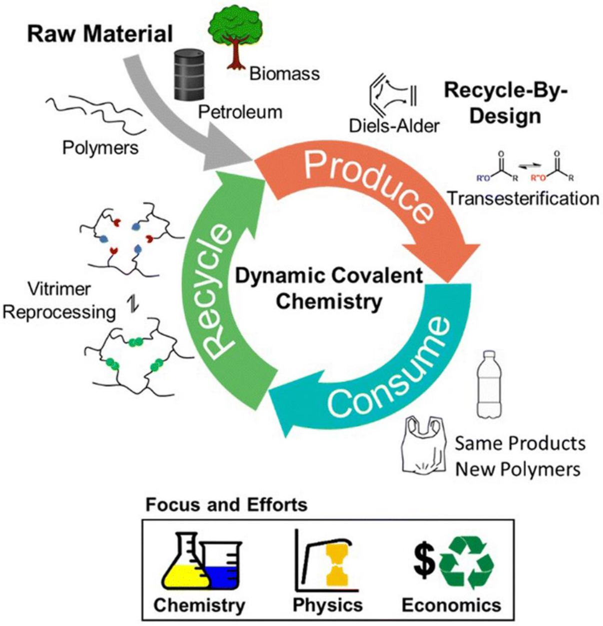

FIGURE 2 - CLOSED-LOOP CIRCULARITY PROVIDED BY DYNAMIC COVALENT CHEMISTRIES LEADS TO INCREASED RETENTION OF PLASTICS IN THE PRODUCTION AND CONSUMPTION CYCLE [16]

1.1 Vitrimers: fundamental science, chemical architecture and properties

The historical classification of polymers has long been governed by a binary distinction between thermoplastics and thermosets, a division based primarily on the nature of their internal cross-linking and their subsequent response to thermal stimuli. Thermoplastics consist of linear or branched macromolecular chains held together by physical entanglements and intermolecular forces, allowing them to flow upon heating and solidify upon cooling, thereby facilitating recyclability but often at the cost of dimensional stability and solvent resistance. [1, 2] In contrast, thermosets are defined by a permanently cross-linked covalent network that provides exceptional mechanical strength, thermal stability, and resistance to environmental degradation. However, their irreversible nature renders them infusible and insoluble, posing severe challenges for repair, reprocessing, and end-of-life management. [3, 4]

The emergence of vitrimers in 2011, introduced by Ludwik Leibler and his colleagues at the École Supérieure de Physique et de Chimie Industrielles (ESPCI) in Paris, represents a fundamental paradigm shift in polymer science by defining a third class of materials that combines the robust performance of thermosets with the malleable processing characteristics of thermoplastics through the implementation of associative dynamic covalent chemistry. [1, 5, 6]

1.1.1 Theoretical foundation of vitrimeric behavior

The conceptual origin of vitrimers lies in the attempt to replicate the unique rheological behavior of inorganic glass-formers, such as vitreous silica, within organic polymer networks. Unlike traditional covalent networks, which are static, vitrimers are classified as covalent adaptable networks (CANs) that maintain a constant degree of chemical connectivity, while allowing for topological rearrangement under specific stimuli. While thermal activation is the most conventional trigger, network rearrangement can also be induced by other external inputs. These include photochemical stimuli, which offer precise spatial control through UV or visible light, chemical triggers such as pH variations or solvent-assisted catalysis, and even electrical or magnetic fields that generate localized heating within the polymer matrix. [7, 8, 10]

<u>Associative vs. dissociative mechanisms</u>

A critical distinction within the realm of CANs is the mechanism of bond exchange. CANs are broadly classified into two groups: dissociative and associative (Figure 3). In a dissociative network, the existing cross-link must first break before a new one can form. This sequence leads to a temporary reduction in cross-link density during the exchange process, resulting in a sudden drop in viscosity and a potential loss of structural integrity, if the material is heated too rapidly. [1, 9, 11]

Vitrimers, instead, are strictly defined by their associative exchange mechanism. In an associative exchange, a new covalent bond is formed between a reactive moiety and an existing cross-link before the original bond is cleaved. This ensures that the total number of cross-links in the network remains constant throughout the reorganization process. This "constant connectivity" prevents the material from dissolving in chemically inert solvents even at high temperatures, distinguishing vitrimers from thermoplastics, which simply melt. [1, 12, 13]

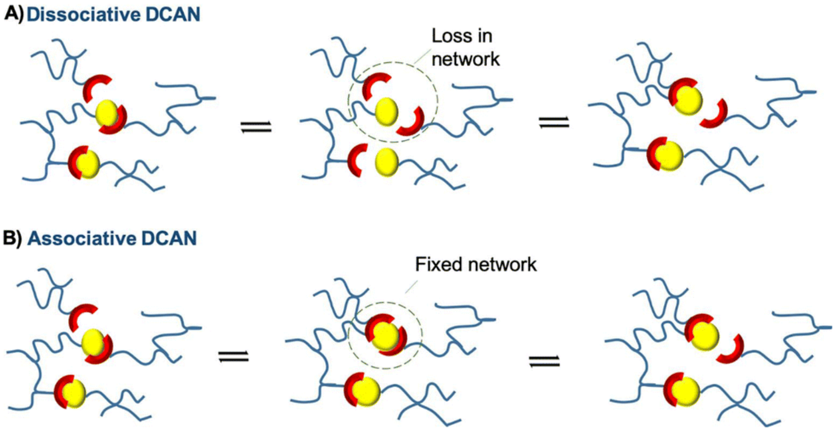

FIGURE 3 - DISSOCIATIVE (A) AND ASSOCIATIVE (B) EXCHANGE IN DYNAMIC COVALENT ADAPTIVE NETWORKS [16]

The most striking feature of vitrimers is their rheological profile, which deviates from the Williams-Landel-Ferry (WLF) model, typically observed in thermoplastic melts, and instead follows the Arrhenius law. This behavior is a direct consequence of the exchange kinetics being the rate-limiting step for macroscopic flow. As temperature increases, the rate of bond exchange increases exponentially, leading to a predictable and gradual decrease in viscosity that allows vitrimers to be processed like vitreous silica. In this context, the activation energy (Ea) of the bond exchange reaction determines how sensitive the material's fluidity is to temperature changes. High Ea values imply a more abrupt transition to flow, whereas low Ea values result in a broader processing window. [1, 14]

1.1.2 Transesterification-based vitrimers

One of the most widely studied associative mechanisms of bond exchange is transesterification. Transesterification-based systems rely on the reaction between ester groups and free hydroxyl groups. The chemical equilibrium is represented as follows:

$$R - COOR' + R'' - OH \overset{\overset{\Delta}{catalyst}}{\Longleftrightarrow} R - COOR'' + R' - OH$$

To achieve practical relaxation times, these systems generally require high temperatures (typically > 150°C) and the presence of catalysts. [5, 6, 14]

The ability of vitrimers to rearrange their network and, consequently, relax stresses resulting from deformations, confers upon them unique functional properties, such as healing capability, shape-memory behavior, recyclability, and reprocessability. [13, 15]

- *Healing capability*: Unlike traditional thermosets, which suffer permanent damage upon fracturing, vitrimers exhibit intrinsic healing. When the material is subjected to heat, the rate of bond breaking and reforming increases, allowing polymer chains to migrate across damaged interfaces and restore structural continuity. This process restores the network’s integrity without a loss in crosslink density. [1]
- *Shape-memory behavior*: Vitrimers demonstrate sophisticated shape-memory effects (SME). The permanent shape is established during the initial curing; however, they can be programmed into a temporary shape and later "re-programmed" into a new permanent shape through viscoelastic relaxation. By heating the material, internal stresses are relaxed, effectively "resetting" the reference equilibrium state of the polymer chains. [2]
- *Reprocessability and recyclability*: Traditional thermosets are notorious for being non-recyclable due to their permanent chemical architecture. Transesterification-based vitrimers solve this dilemma through thermal activation. At elevated temperatures, the rate of bond exchange increases significantly, allowing the material to be ground into powder and re-molded via injection molding or compression molding, processes typically reserved for thermoplastics. [3] This “mechanical recyclability” ensures that the material can be reused multiple times while retaining high mechanical performance. [4]

1.1.3 Bio-based vitrimers

In the last five years, further efforts toward sustainability and circularity have been carried out through the design, synthesis, and characterization of bio-based vitrimers; these are materials that derive from biosources (i.e., bio-based monomers/chemicals) and exploit the same chemistries involved in the formation of non-biobased dynamic CANs.

The transition from fossil-based to bio-based vitrimers represents a significant leap toward sustainable polymer engineering. By utilizing renewable feedstocks, such as lignin, cellulose, starch, vegetable oils, and agricultural waste, bio-based vitrimers drastically reduce the industry's dependence on depleting fossil fuels and minimize the overall carbon footprint.

One of the most compelling advantages of these materials is their superior environmental profile: they offer lower greenhouse gas emissions during production and provide versatile end-of-life pathways, including potential biodegradability and compostability in closed-loop systems. Furthermore, the synthesis of bio-based vitrimers often utilizes less harmful monomers and green solvents, reducing human and environmental toxicity. While fossil-based alternatives currently benefit from established scalability and lower initial production costs, bio-based vitrimers are increasingly matching (and in some cases, surpassing) the mechanical performance of their synthetic counterparts. Despite existing challenges regarding moisture sensitivity and the need for optimized large-scale processing, the integration of biomass pre-treatment and refined monomer synthesis is positioning bio-based vitrimers as the high-performance, eco-friendly successors to traditional dynamic networks. [16]

Transesterification-based green vitrimers

Among the various associative mechanisms of dynamic bond exchange, transesterification has emerged as a prominent candidate for the development of sustainable, bio-based vitrimers. In the context of green chemistry, the abundance of ester groups in natural precursors makes this exchange reaction ideal for creating dynamic networks from renewable resources.

A significant example of bio-derived vitrimer based on transesterification chemistry involves the use of *acrylated epoxidized cottonseed oil* (AECO), which enables the fabrication of reprocessable coatings through the reaction between ester and hydroxyl groups at elevated temperatures in the presence of a catalyst. [42] Another widely investigated system combines monomers derived from glycerol (HPPA), soybean oil (AESO), and hemicellulose (THFMA), resulting in materials with excellent self-healing, weldability, and shape-memory capabilities. [43] Vanillin-based vitrimers (DGEVADMA) in combination with glycerol have also been developed, exhibiting remarkable welding efficiency and the potential for chemical recycling via ethanol-mediated alcoholysis. [27] Further research illustrates external catalyst-free epoxy vitrimers produced by incorporating glycerol into epoxy-anhydride systems, where the glycerol-derived hydroxyl groups act as both reactants and intrinsic promoters for dynamic bond exchange. [44] Finally, another representative example is provided by the combination of *glycerol 1,3-diglycerolate diacrylate* (GDGDA) and THFMA, which yields a bio-derived vitrimer ideally suited for DLP 3D printing, characterized by high double-bond conversion and thermally activated topological network rearrangements. [28]

1.2 Additive manufacturing

Additive manufacturing (AM), frequently referred to as 3D printing, comprises a suite of technologies that enable the fabrication of complex three-dimensional objects through the sequential, layer-by-layer deposition of material. This manufacturing paradigm translates digital designs from computer-aided design (CAD) software into physical components, typically through an intermediary "slicing" process that defines two-dimensional layers for the printer to execute. In contrast to subtractive machining, which relies on cutting tools to remove material, AM utilizes energy sources (such as lasers, electron beams and ultraviolet light) or specialized binding agents, to solidify the material. Once a single cross-section is completed, the build platform adjusts by a specific layer thickness, allowing the subsequent layer to be applied. This iterative sequence persists until the three-dimensional geometry is fully realized. [17] Since its inception in the 1980s for rapid prototyping, AM has transitioned into a pivotal technology within Industry 4.0, finding critical applications in the aerospace, biomedical, automotive, and electronics sectors. [18]

The technological adoption of AM is driven by several strategic advantages over traditional subtractive or formative methods. These include:

- *Design freedom*: AM facilitates the creation of unprecedentedly intricate geometries and lightweight lattice structures that are either unachievable or prohibitively expensive via conventional machining.
- *Waste minimization*: By adding material only where structurally requisite, AM significantly reduces raw material waste, compared to subtractive techniques.
- *Customization*: AM technology enables high levels of personalization and rapid production for small batches without the need for dedicated molds, thereby accelerating the development-to-market timeline.
- *Circular Economy*: The integration of recycled polymers and bio-derived materials aligns AM with sustainability goals and resource efficiency. [19]

The additive manufacturing (AM) process is systematically categorized into seven distinct phases, ranging from initial digital design to final post-processing (Figure 4).

- *Phase 1* - *CAD modeling and digital design*: The foundational stage of the AM workflow involves the creation of a three-dimensional (3D) digital model. This is primarily achieved through computer-aided design (CAD) software. In instances where an original design is unavailable, reverse engineering techniques, such as 3D scanning tools, may be employed to reconstruct the geometry of an existing physical object. [17]
- *Phase 2* - *Conversion to STL format*: Following the design phase, the CAD model must be converted into the standard tessellation language (STL) format. This format represents the

3D object's surface geometry as a mesh of triangular facets, each defined by their specific vertices and normals. [17]

- *Phase 3* - *Model slicing*: Given that additive manufacturing is a stratified fabrication process, the STL model is computationally partitioned into numerous cross-sections, known as layers. The physical printing process proceeds by depositing or curing these layers sequentially, building each new stratum upon the preceding one until the geometry is complete. [17]
- *Phase 4* - *Toolpath generation and G-code*: Once the model is sliced, a toolpath is generated and translated into G-code. This standardized numerical control language provides the additive manufacturing system with the precise instructions necessary to execute the layer-by-layer construction of the part. [17]
- *Phase 5* - *Machine configuration and fabrication*: Prior to the commencement of the build, the AM hardware requires precise configuration. Critical operational parameters include material selection, power settings, layer thickness, travel velocity, and support structure integration. Once these settings are established and the process begins, the machinery typically functions autonomously, necessitating only minimal oversight. [17]
- *Phase 6* - *Component removal*: Upon completion of the build cycle, the printed object must be extracted from the system. In most AM modalities, this involves physically separating the component from the build platform. [17]
- *Phase 7* - *Post-processing procedures*: The final stage involves post-processing, the complexity of which varies significantly depending on the specific AM technology and materials utilized. For example, components produced via stereolithography (SLA) require a UV post-curing phase to achieve their final properties. Additionally, any auxiliary support structures, which are essential for preventing layer dropouts in overhanging regions, must be removed. This removal can be performed either through mechanical excision or via chemical dissolution in a compatible solvent that does not compromise the integrity of the primary part. [17]

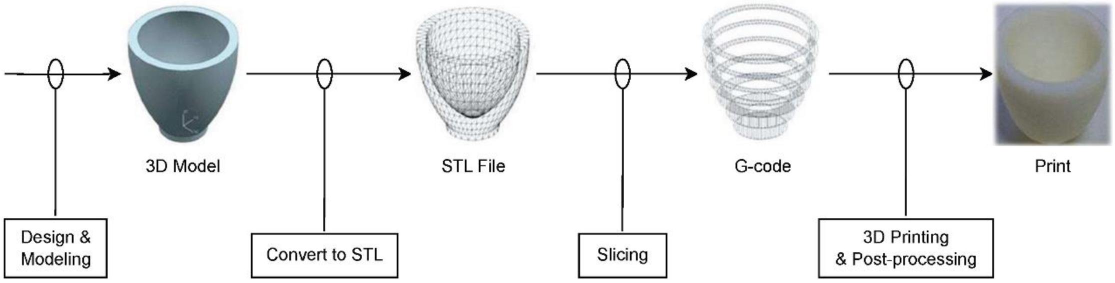

FIGURE 4 - BASIC PRINCIPLES OF AM PROCESSES

The most used techniques for 3D printing of polymer composites (categorized based on the physical state of the feedstock and the consolidation mechanism employed) are:

1. *Material extrusion (MEX)*: The most prevalent method, utilizing a heated nozzle to deposit melted thermoplastic filaments (fused deposition modeling - FDM) or granules (fused granular fabrication - FGF).

2. *Powder bed fusion (PBF)*: selective laser sintering (SLS) involves laser-induced fusion of polymer powder particles, where the surrounding bed provides intrinsic support for complex features.
3. *Material jetting (PolyJet)*: Dispenses and instantly cures photopolymer droplets using UV lamps, enabling sophisticated multi-material fabrication.
4. *Vat photopolymerization (VP)*: Selective curing of liquid photosensitive resins via UV light sources, in the form of a laser beam (stereolithography - SLA), managed by a projection system (digital light processing - DLP) or controlled by a liquid crystal display (LCD), to achieve superior resolution and surface finish. [20]

1.2.1 Photopolymers and vat photopolymerization mechanisms

In this experimental work, LCD 3D printing, a vat photopolymerization technique, was utilized as the additive manufacturing method for the fabrication of vitrimers. In VP, a liquid photopolymer, contained in a reservoir (vat), is selectively cured by light-activated polymerization. [20]

Photopolymers are a specialized class of reactive resins that undergo a phase transition from liquid to solid when exposed to specific wavelengths of light, typically in the ultraviolet (UV) or visible spectrum. This transformation is driven by photopolymerization, a chemical process where light-activated molecules, known as photoinitiators, absorb photons to generate reactive species: free radicals or cations. These species then trigger the chain-growth polymerization of monomers and oligomers, resulting in a highly crosslinked polymer network. Utilizing this principle, consecutive layers of resin are gradually fabricated from a sliced STL file. [21, 22]

Photoinduced processes are generally categorized into two types: free-radical and ionic systems. Both systems follow a three-stage cycle (Figure 5):

1. *Initiation*: The photoinitiator absorbs UV radiation and generates reactive species.
2. *Propagation*: These species react with monomers and oligomers to build long molecular chains.
3. *Termination*: The process ends through mechanisms such as recombination, quenching or disproportion. [23]

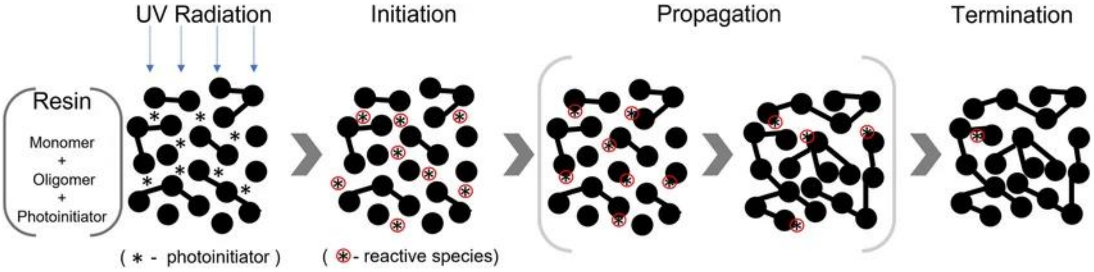

FIGURE 5 - SCHEMATIC OF THE POLYMERIZATION PROCESS OF A PHOTOSENSITIVE RESIN [19]

There are significant differences between these two systems. Free-radical polymerization is a rapid process that typically stops as soon as the light source is removed. It is commonly used for crosslinking monomers like acrylates, styrene, and thiol-ene. In contrast, ionic polymerization (specifically cationic) requires more exposure time, but has the unique ability to continue even after the light is turned off. This method is essential for polymerizing substances like epoxides, ketones, and aldehydes. [19]

1.2.2 Liquid crystal display (LCD) 3D printing technology

Liquid crystal display (LCD) 3D printing, also known as masked stereolithography (mSLA), is a specialized subset of VP. This technology has gained significant traction across both academic and industrial sectors due to its ability to produce high-resolution components with high throughput and enhanced cost-effectiveness.

The fundamental mechanism of LCD 3D printing involves the selective curing of a liquid photopolymer resin via a digital light source. The process is defined by three primary components: an LED array, an LCD screen, and a resin vat (Figure 6).

1. *Light generation*: An array of UV or visible LEDs (the backlight) emits a uniform field of light upward, toward the build area.
2. *Digital masking*: A high-resolution LCD panel, positioned between the LED source and the resin vat, acts as a dynamic spatial light modulator (a digital mask). For each layer of the 3D model, the LCD panel turns specific pixels "on" (transparent) or "off" (opaque), based on the sliced geometry of the part.
3. *Selective polymerization*: The light, passing through the transparent pixels, triggers a photopolymerization reaction in the resin, solidifying an entire layer simultaneously.
4. *Incremental build*: Once a layer is cured, the build platform moves vertically by one layer thickness (25-100 µm), and the process repeats until the object is complete.

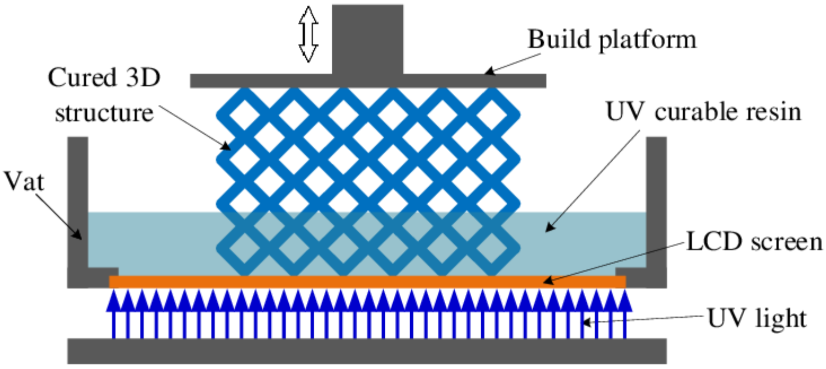

FIGURE 6 - WORKING PRINCIPLE OF THE LCD-TYPE 3D PRINTER [24]

While LCD, SLA, and DLP 3D printing technologies all belong to the vat photopolymerization family, they differ significantly in how they deliver light to the resin (Figure 7):

- SLA is the "gold standard" for precision but operates on a vector-based principle. It utilizes a concentrated UV laser beam, directed by two galvanometers (mirrors), which traces the perimeter and infill of each layer point-by-point. SLA is, therefore, highly precise but generally slower, because the build time is proportional to the volume and complexity of the object. In contrast, LCD prints an entire layer at once, meaning build time is only dependent on height. [24]

- DLP uses a digital projector (DMD - digital micromirror device) to flash the image of each layer all at once, offering a good balance between speed and resolution. Light is projected from a single point source through a lens, which can sometimes cause minor optical distortions (parallax) at the edges of the build plate, while LCD uses a parallel LED array directly beneath the vat, providing a more uniform light path across the entire building area.

LCD screens are considered "consumables" because the high-intensity UV light eventually degrades the liquid crystals. However, the absence of expensive optical and projection components, standard in SLA and DLP technologies, makes LCD 3D printers more cost-effective, with broader accessibility for laboratories. [24]

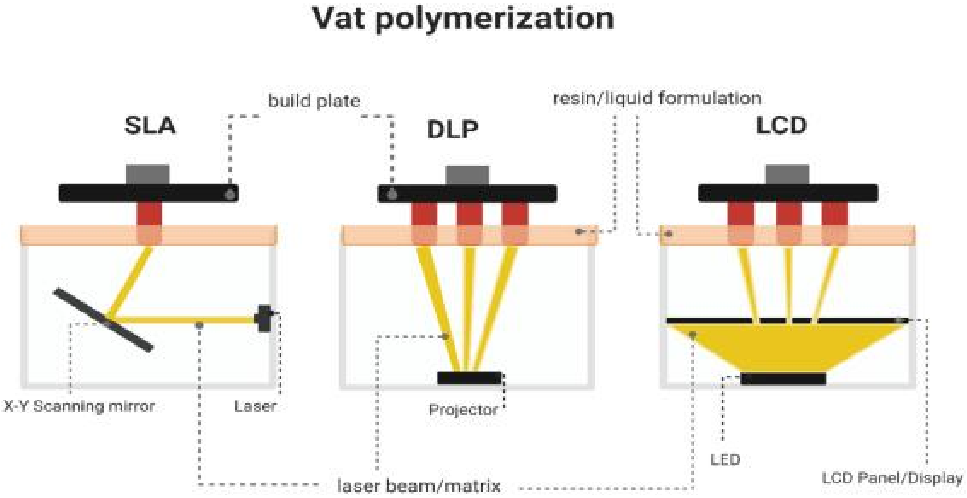

FIGURE 7 - SCHEMATIC COMPARISON OF SLA, DLP, AND LCD 3D PRINTING TECHNOLOGIES, HIGHLIGHTING THE DIFFERENCES IN LIGHT SOURCE AND LAYER PATTERNING MECHANISMS [24]

2. Materials and methods

This chapter provides a comprehensive examination of the materials and experimental methodologies employed throughout this study.

2.1 Materials

2.1.1 Glycerol 1,3-diglycerolate diacrylate (GDGDA)

Glycerol (also known as *propane-1,2,3-triol*) has become a fundamental resource for sustainable chemistry, owing to its abundance as an industrial byproduct and its versatile chemical properties. As depicted in Figure 8, glycerol finds extensive use across several sectors, spanning from the pharmaceutical and personal care fields to the production of polymers. [25]

The transition of glycerol from a simple industrial byproduct to a high-value platform chemical facilitates the production of sustainable polymers. By chemically modifying this green building block to make it cross-linkable, glycerol significantly mitigates the environmental impact associated with traditional petroleum-based thermosets. [25, 26, 27]

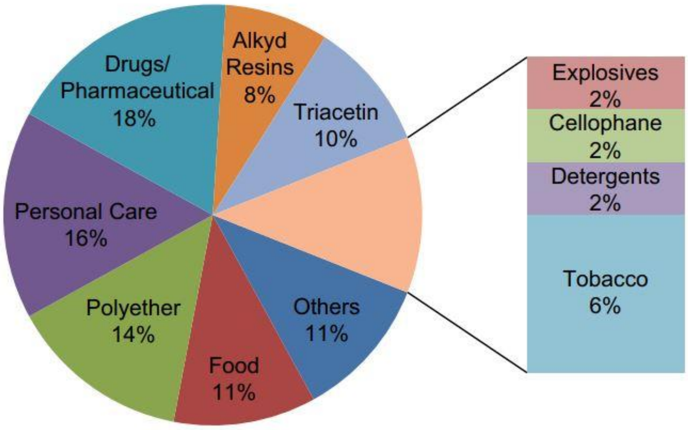

FIGURE 8 - GLYCEROL INDUSTRIAL APPLICATIONS [25]

<u>Industrial production of glycerol</u>

Glycerol is primarily generated as a byproduct of the oleochemical and biodiesel industries through the processing of triglycerides. [25] The three dominant industrial pathways are:

- *Transesterification*: Currently the most prevalent source due to the expansion of the biodiesel sector. In this reaction, triglycerides react with an alcohol (typically methanol) in the presence of a catalyst to produce fatty acid methyl esters (biodiesel) and glycerol. Quantitatively, producing 100 kg of biodiesel yields approximately 10 kg of crude glycerol.
- *Saponification*: Utilized in the soap-making industry, this process involves the hydrolysis of fats and oils with an alkali (e.g., sodium hydroxide), resulting in the formation of soap and the liberation of glycerol.
- *Hydrolysis*: Triglycerides react with water (steam) to yield free fatty acids and glycerol, often referred to, in this context, as "sweetwater".

Regardless of the method, the resulting crude glycerol contains various impurities, such as water, salts, and unreacted molecules, necessitating refinement through techniques like vacuum distillation or ion-exchange to achieve the high purity levels required for industrial chemical synthesis. [25]

<u>GDGDA as a sustainable precursor in vitrimer science</u>

Glycerol 1,3-diglycerolate diacrylate (GDGDA) is a commercially available, bio-based monomer that has emerged as a critical precursor in the development of sustainable, high-performance polymers, particularly vitrimers. GDGDA features a glycerol fragment in its molecular backbone, making it an environmentally friendly alternative to traditional petroleum-based acrylates. [28]

The molecular architecture of GDGDA (Figure 9) is characterized by the presence of both hydroxyl (-OH) and ester groups, which are fundamental to its functionality. These groups enable the material to undergo thermoactivated transesterification reactions, a type of dynamic covalent chemistry that allows the resulting polymer network to rearrange its topology without losing its integrity. In these systems, the ester groups (often from co-monomers) are exchanged with the hydroxyl groups of the GDGDA fragments, facilitating stress relaxation at elevated temperatures. [28]

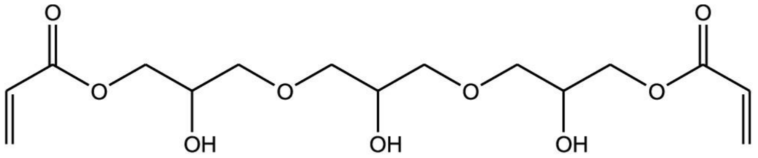

FIGURE 9 - CHEMICAL STRUCTURE OF GLYCEROL 1,3-DIGLYCEROLATE DIACRYLATE (GDGDA)

GDGDA is highly suitable for 3D printing, due to its rapid free radical polymerization rate. [27, 28] Moreover, polymers synthesized using GDGDA fragments often exhibit unique thermal and mechanical profiles:

- *Thermal characteristics*: Due to the long and flexible alkyl chains in the GDGDA fragment, the resulting vitrimers can possess a low glass transition temperature (Tg). Despite this, the materials remain solid at room temperature.
- *Shape memory*: GDGDA-based vitrimers demonstrate excellent shape memory capabilities. These polymers can be programmed into temporary shapes and then return to their permanent shape with a 100% recovery ratio upon reheating. [28]
- *Weldability and repairability*: The dynamic nature of the GDGDA network allows for the welding and repair of broken components. Thermal treatment (e.g., at 180 °C) triggers bond exchange at the interface, often resulting in mechanical properties that can surpass the original sample due to additional hydrogen bonding and network rearrangement. [28]

For this research, *glycerol 1,3-diglycerolate diacrylate* was acquired from Merck. It appears, at ambient temperature, as a transparent, viscous liquid with a density of 1.18 g/mL. [36]

2.1.2 Acrylated epoxidized soybean oil (AESO)

In the pursuit of sustainable polymer chemistry, vegetable oils (VOs) have emerged as one of the most promising renewable feedstocks due to their inherent biodegradability, low toxicity, and high availability. In recent years, these bio-based monomers have gained significant traction in additive manufacturing, particularly in vat photopolymerization, as they offer a "green" alternative to petroleum-derived resins without compromising the structural integrity of the final 3D-printed parts. [30].

Structurally, VOs are triglycerides composed of three fatty acids chains joined together to a glycerol unit. Fatty acid chains can exhibit varying degrees of unsaturation, which serve as versatile reactive sites for chemical modification. [29]

Among these derivatives, *acrylated epoxidized soybean oil* (AESO) stands out as a key monomer in the synthesis of bio-based resins and vitrimers. AESO is synthesized through the epoxidation and acrylation of soybean oil, extracted from soybean seeds. This process, schematized in Figure 10, introduces highly reactive acrylate functional groups onto the triglyceride backbone, which enable rapid free-radical photopolymerization when exposed to UV or visible light in the presence of a suitable photoinitiator. The long aliphatic chains of soybean oil provide the resulting polymer with inherent flexibility and impact resistance, while the multi-functional nature of the AESO molecule allows for the formation of a robust, crosslinked network. [31]

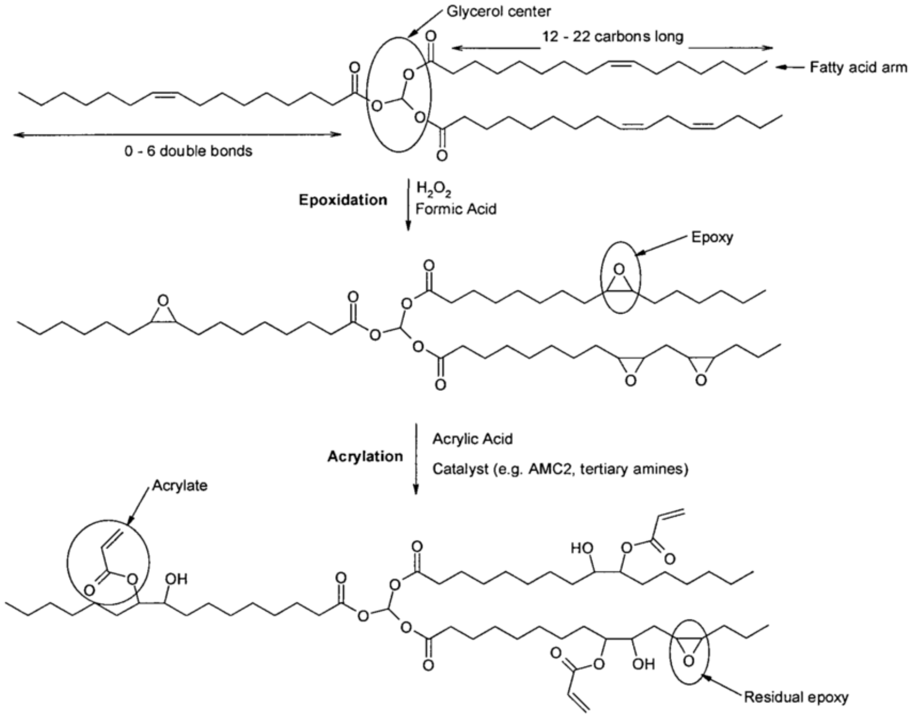

FIGURE 10 - CHEMICAL STRUCTURE OF AESO AFTER EPOXIDATION AND ACRYLATION OF SOYBEAN OIL [31]

The *acrylated epoxidized soybean oil* (AESO) monomer, utilized in this research, was acquired from Merck. At ambient temperature, it appears as viscous fluid with a characteristic amber coloration and a density of 1.04 g/ml. [32]

2.1.3 Ethyl(2,4,6-trimethylbenzoyl)phenylphosphinate (TPOL)

In the development of light-activated resin systems, *ethyl(2,4,6-trimethylbenzoyl)phenylphosphinate* (Figure 11), commonly designated as TPOL (or TPO-L), functions as a highly efficient Type I photoinitiator. [27] Unlike Type II systems, which necessitate a co-initiator, TPOL undergoes a unimolecular bond cleavage upon exposure to electromagnetic radiation, primarily within the UV-A and visible blue light spectrum (365–420 nm). [34] This specific initiation range ensures high compatibility with modern LCD 3D printing technologies, which typically utilize LED arrays centered at 405 nm. [35]

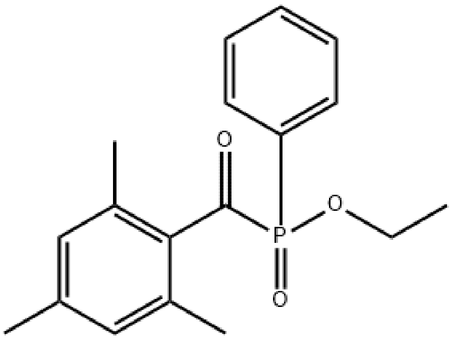

FIGURE 11 - CHEMICAL STRUCTURE OF ETHYL(2,4,6-TRIMETHYLBENZOYL)PHENYLPHOSPHINATE (TPOL)

From a mechanistic perspective, the absorption of photons triggers the homolytic cleavage of the C-P bond, generating two highly reactive radicals: the benzoyl and the phosphinoyl species. The latter is particularly effective at initiating the polymerization of acrylates, such as AESO, due to its high reactivity and reduced sensitivity to oxygen inhibition, compared to traditional initiators. [33] Furthermore, TPOL is frequently preferred in experimental formulations because of its liquid state at room temperature, which simplifies the blending process, and its low-yellowing characteristics, preserving the optical clarity of the final 3D-printed structures. [27]

For the purposes of this research, TPOL was procured from Merck. At ambient temperature, it is characterized by a density of 1.14 g/mL. [37]

2.1.4 Phosphate methacrylate (Miramar A99)

Miramar A99 (a *phosphate methacrylate* monomer, also referred to as Miramer A99) is utilized as a high-performance transesterification catalyst, specifically designed for the synthesis of bio-based vitrimers through digital light processing (DLP) 3D printing.

A primary advantage of this catalyst is its excellent solubility in acrylate and methacrylate monomers, which ensures a homogeneous resin formulation without the need for additional solvents. Unlike traditional additives, Miramar A99 is covalently incorporated into the photopolymer network during the curing process, preventing leaching and maintaining the structural integrity of the material. Its functional role is critical for enabling the thermoactivated dynamic bond exchange between hydroxyl and ester groups; by triggering these exchange reactions at elevated temperatures, Miramar A99 facilitates rapid stress relaxation and topological network rearrangements. In specific vitrimeric systems, such as those composed of *glycerol 1,3-diglycerolate diacrylate* (GDGDA) and *tetrahydrofurfuryl methacrylate* (THFMA), the inclusion of Miramar A99 has been shown to significantly reduce relaxation times as temperature increases, thereby imparting essential functionalities such as weldability, repairability, and 100% shape-memory recovery. [28]

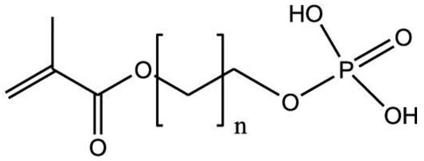

FIGURE 12 - CHEMICAL STRUCTURE OF PHOSPHATE METHACRYLATE (MIRAMAR A99)

For this experimental study, Miramer A99, whose chemical structure is illustrated in Figure 12, was sourced from Miwon Specialty Chemical. At ambient temperature, it appears as clear, viscous liquid with a greenish hue and a density of 1.25 g/ml. [38]

2.2 Methods

2.2.1 Preparation of the investigated resins for LCD 3D printing

Various formulations based on *glycerol 1,3-diglycerolate diacrylate* (GDGDA, referred to as 'Gly') and *acrylated epoxidized soybean oil* (AESO) were investigated. According to the safety data sheets provided by Merck, the glycerol was stored under refrigeration at a temperature of 4°C, while all other reagents were kept at ambient temperature. The blends were prepared by manually mixing the two bio-based monomers (Gly/AESO) in different ratios, followed by the addition of 1 phr of the photoinitiator *ethyl(2,4,6-trimethylbenzoyl)phenylphosphinate* (TPOL) and 5 phr of the *phosphate methacrylate* catalyst (Miramar A99).

Specifically, to demonstrate the necessity of the Miramar A99 catalyst and its influence on the transesterification reaction, the formulation containing 80% glycerol and 20% soybean oil (Gly/AESO:80-20) was investigated in two additional variants: one without the catalyst (Gly/AESO:80-20-0A99) and another containing 2.5 phr of the catalyst (Gly/AESO:80-20-2.5A99).

To designate each formulation, acronyms were used, as detailed in the following Table 1.

TABLE 1 - DESCRIPTION OF THE FORMULATIONS AND ASSOCIATED ACRONYMS

Acronyms	Formulations
Gly/AESO:90-10	*Glycerol/AESO* (90/10 %wt) + 1 phr *TPOL* + 5 phr *A99*
Gly/AESO:80-20	*Glycerol/AESO* (80/20 %wt) + 1 phr *TPOL* + 5 phr *A99*
Gly/AESO:80-20-0A99	*Glycerol/AESO* (80/20 %wt) + 1 phr *TPOL*
Gly/AESO:80-20-2.5A99	*Glycerol/AESO* (80/20 %wt) + 1 phr *TPOL* + 2.5 phr *A99*
Gly/AESO:70-30	*Glycerol/AESO* (70/30 %wt) + 1 phr *TPOL* + 5 phr *A99*
Gly/AESO:60-40	*Glycerol/AESO* (60/40 %wt) + 1 phr *TPOL* + 5 phr *A99*

2.2.2 LCD 3D printing

The specimens were 3D printed using an LCD 3D printer, specifically the *Phrozen Sonic Mini 8K* (Phrozen Tech Co. Ltd., Hsinchu, Taiwan – Figure 13). This system utilizes a liquid crystal display (LCD) acting as a digital mask to selectively cure layers of photosensitive resin.

The defining characteristic of this device is its ultra-high spatial resolution: it is equipped with a 7.1-inch monochromatic LCD panel with a pixel density of 1152 ppi, resulting in an XY resolution of 22 µm. This allows for the reproduction of intricate geometries and minimizes the "stair-stepping" effect common in additive manufacturing.

The system employs a linear projection LED module with an intensity of 1.8 mW/cm² at visible wavelength of 405 nm. Unlike standard matrix arrays, this optical engine enhances light uniformity and ensures that the UV intensity is distributed consistently across the entire building plate.

The effective building envelope is 16.5 cm (l) x 7.2 cm (w) x 18 cm (h), with layer thickness (Z resolution) adjustable from 0.01 to 0.30 mm. Furthermore, the compact dimensions of the resin vat facilitate low-volume material consumption, permitting iterative prototyping and preliminary testing while significantly reducing feedstock waste and preparation overhead.

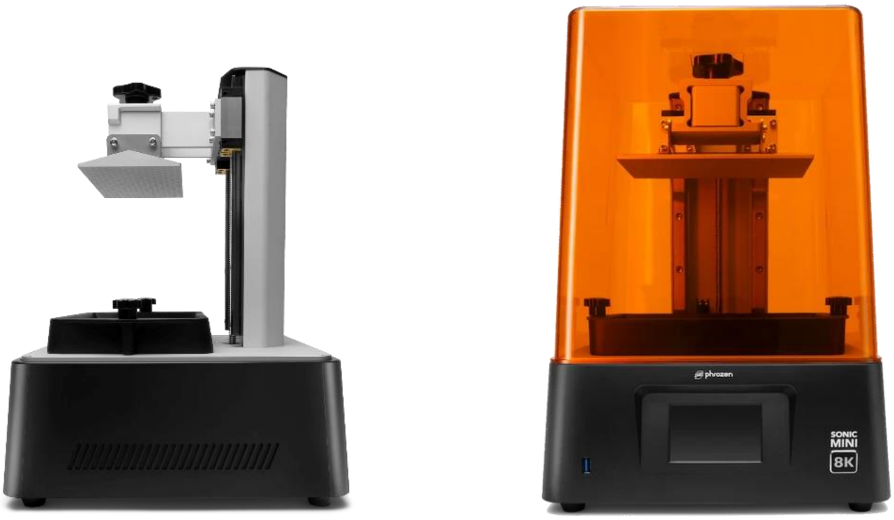

FIGURE 13 - PHROZEN SONIC MINI 8K

The digital models, initially generated as STL files, were processed using CHITUBOX (v.1.1.0, Chitu Systems), the dedicated slicing software for the Phrozen ecosystem. As the computational bridge between the CAD geometry and the printer hardware, the slicer was employed to discretize the 3D models into a series of 2D cross-sectional layers.

In addition, the software enables the precise determination of part positioning and orientation, the generation or removal of support structures, including the customization of their geometry and dimensions, and the calibration of platform kinematics between successive layers. It also allows for the fine-tuning of critical printing parameters, specifically exposure time and layer thickness.

Jacob's working equation and 3D printing parameters optimization

To calibrate the printing process for the specific resin formulation, the curing characteristics were systematically quantified following the theoretical framework established by *Jacob's working equation*. This procedure was essential to determine the *critical exposure* (Ec) and the *penetration depth* (Dp) of the UV light within the material.

The experimental workflow consisted of the following steps:

1. Several circular specimens (with a diameter of 8 mm) were fabricated individually and printed directly onto the FEP (*fluorinated ethylene propylene*) film at the base of the resin vat. To isolate the effects of light-material interaction, the mobile build platform was bypassed during this procedure. Between consecutive print cycles, the *exposure time* (t_{exp}) was the sole experimental variable. Consequently, the thickness of the resulting samples is governed exclusively by the programmed exposure duration, eliminating any mechanical influence or constraints imposed by the Z-axis positioning. Given that the UV *light intensity* (I) is constant for this printer model, each specimen is subjected to a specific *radiant exposure* (E), which is directly proportional to the exposure time according to the following relation (Equation 1):

   $$E = I * t_{exp} \tag{1}$$

2. After printing, the specimens were delicately recovered from the resin vat and carefully cleaned with *isopropyl alcohol* (IPA), to remove unreacted monomer, and dried. The thickness of each specimen (Cd) was measured using a high-precision digital caliber at multiple points to ensure statistical consistency.
3. The experimental data were analyzed by plotting the measured *cure depth* (Cd) against the natural logarithm of the applied *radiant exposure* (E). According to *Jacob's working equation* (Equation 2):

   $$C_d = D_p * \ln\left(\frac{E}{E_c}\right) \tag{2}$$

   Where:

- Dp [mm], the *penetration depth*, represents the slope of the working curve, indicating the resin's sensitivity to light attenuation;
- Ec [mJ/cm²], the *critical exposure*, is the X-intercept of the curve, representing the minimum energy required to induce gelation.

4. *Jacob's working curve* was generated via linear regression of the experimental points. This methodological approach allowed for the analytical derivation of the optimal exposure times required to achieve the target layer thickness for the subsequent experimental phases.

Generally, following the fabrication process, all produced components (ranging from various specimen types to complex geometrical structures) were thoroughly washed in *isopropyl alcohol* (IPA) and subsequently air-dried at room temperature. The residual resin was collected and stored in specialized light-shielded containers to prevent unintended photopolymerization, ensuring its viability for subsequent printing cycles or further characterization tests.

2.2.3. Viscosity analysis

The rheological properties of the photosensitive resins were characterized using a high-precision *Anton Paar MCR 702e Multidrive* rheometer (Graz, Austria – Figure 14). To ensure accurate data acquisition, all measurements were conducted at a stabilized temperature of 25°C, maintained via a water circulation cooling system coupled with the thermal control unit. The experimental setup utilized a parallel-plate geometry (25 mm diameter), with a measurement gap accurately set at 0.300 mm. This narrow gap was selected to simulate the fluid dynamics and the confinement conditions typically encountered during the resin replenishment phase in the LCD printing process.

The materials flow behavior was evaluated through rotational steady-state shear tests: the *dynamic viscosity* (η) was recorded in [mPa·s] as a function of the *shear rate* ($\dot{\gamma}$), which was varied logarithmically across an interval ranging from 0.1 to 100 s^{-1}.

FIGURE 14 - ANTON PAAR MCR 702E MULTIDRIVE RHEOMETER (GRAZ, AUSTRIA)

2.2.4 Photocuring kinetics analysis

The curing kinetics and reactivity of the various resin formulations were investigated via real-time photorheology test (time-sweep experiment), using the *Anton Paar MCR 702e Multidrive* system (Graz, Austria). The experiments were performed by positioning the sample between two parallel plates and applying a small-amplitude oscillatory deformation to probe its evolving mechanical properties. This configuration enables continuous acquisition of the elastic component, the *storage modulus* (G′), and the viscous component, the *loss modulus* (G″), while polymerization proceeds.

A dedicated irradiation system delivering visible light was integrated into the rheometer, allowing simultaneous exposure of the material and monitoring of its viscoelastic response. Throughout the time-sweep analysis, the specimen was subjected to constant illumination, and its transition from an initially fluid state to a crosslinked network was followed in real time.

At the beginning of the experiment, the formulation exhibited predominantly viscous behavior, characteristic of low-viscosity liquids (G’’ > G’). Upon activation by light, network formation progressively increased the elastic contribution, as evidenced by a marked rise in the storage modulus (G’). The gelation threshold (*gel point*) was identified at the crossover between G’ and G” curves, corresponding to the shift from the viscous-liquid to the solid-like mechanical behavior.

All measurements were carried out using the Anton Paar rheometer operating in a parallel-plate geometry (25 mm diameter) with a quartz lower plate, to facilitate bottom-up UV transmission. The plate gap was maintained at 300 µm, and the temperature was controlled at 25 °C for the entire duration of the tests. Oscillatory time-sweep experiments were conducted within the linear viscoelastic domain, previously determined by amplitude-sweep analysis, using a fixed strain amplitude of 1% and an angular frequency of 1 Hz. Following a short stabilization period of 30 s, irradiation was initiated from beneath the sample using an UV source operating at a wavelength of 405 nm. The analysis was concluded once the G’ profile reached a plateau, indicating the completion of the cross-linking reaction. The temporal evolution of both viscoelastic moduli was analyzed to quantify the kinetics of crosslinking and to assess the mechanical performance achieved after full curing.

2.2.5 Fourier transform infrared (FTIR) spectroscopy

Chemical characterization and monitoring of the polymerization process were conducted using *Fourier transform infrared* (FTIR) spectroscopy. This non-destructive analytical technique is based on the interaction between the infrared radiation and the material’s molecular structure, according to the physical principle whereby, when a sample is exposed to IR radiation, it absorbs specific wavelengths that correspond to the vibrational frequencies of its chemical bonds (such as stretching or bending modes).

The "Fourier transform" aspect refers to the mathematical process that converts raw interferogram data, acquired with a Michelson interferometer, into a readable spectrum. The resulting spectrum, which plots *absorbance* against the *wavenumber* $[\mathrm{cm}^{-1}]$, serves as a unique molecular fingerprint of the specimen, allowing for the identification of functional groups and the monitoring of chemical transformations.

For the analysis of both liquid resins and solid 3D-printed specimens, a *Thermo Scientific Nicolet iS20 FTIR* spectrometer (Figure 15) was operated in *attenuated total reflection* (ATR) mode. Unlike traditional transmission FTIR, which often requires complex sample preparation, ATR allows for the direct analysis of samples in their natural state. The principle of ATR relies on the internal reflection of the IR beam within a high-refractive-index crystal (typically diamond or germanium) in contact with the sample. This reflection generates an evanescent wave that penetrates the sample surface to a limited depth (typically 0.5 to 5 µm). The intensity of this wave is attenuated in spectral regions where the sample absorbs energy, enabling high-resolution surface analysis.

FIGURE 15 - THERMO SCIENTIFIC NICOLET IS20 FTIR SPECTROMETER

All spectra were collected in air, with a scanning speed of one scan every 1.2 seconds and a spectral resolution of 4 cm^{-1}, and processed using the Thermo Scientific OMNIC Spectra software. The conversion of reactive functional groups, specifically the (C = C) double bonds associated with the acrylate groups, was quantified by analyzing the spectral changes at the wavenumber of 1635 cm^{-1}, before and after photopolymerization. The *degree of conversion* (DC) of the formulations was then calculated according to the following Equation 3:

$$DC_{\%} = \left(1 - \frac{A_{post}}{A_{pre}}\right) * 100 \tag{3}$$

Where:

- Apre is the peak area of the functional group before curing;
- A$post$ is the peak area of the functional group after curing.

2.2.6 Stress-Relaxation tests

The stress-relaxation test is a transient rheological method employed to characterize the time-dependent viscoelastic behavior of cross-linked polymers. In this test, a constant *shear strain* (γ_0) is applied to the specimen. The resulting *stress* (σ) is monitored as it decays over time due to internal molecular rearrangements and, in the case of dynamic networks, bond exchange reactions.

This type of analysis needs to be conducted at elevated temperatures (150-180°C). This thermal activation is required to trigger the dynamic bond-exchange mechanisms, via transesterification, within the polymer network, which are otherwise “frozen” at ambient conditions. Monitoring the stress decay at these temperatures allows for the determination of the *relaxation time* (τ*) and the subsequent calculation of the *activation energy* barrier (Ea) associated with the material's topological rearrangement.

The primary parameter of interest is the *relaxation modulus*, G(t), calculated as the ratio between the time-dependent stress and the applied strain (Equation 4):

$$G(t) = \sigma(t)/\gamma_0 \tag{4}$$

This test is crucial for identifying the *relaxation time* (τ*), which represents the time required for the modulus to decay, at a specific temperature, to 1/e (approximately 37.8%) of its initial value.

Stress-relaxation measurements were performed using the *Anton Paar MCR 702e Multidrive* rheometer (Graz, Austria) with an 8 mm parallel-plate geometry. The specimens were 3D-printed disks with a diameter of 8 mm and a thickness of 2 mm.

A constant shear strain of 0.5% was applied, ensuring that all measurements remained within the *linear viscoelastic region* (LVR), and a constant compressive normal force of 0.25 N was maintained throughout the test to ensure optimal contact between the plates and the specimen, compensating for any thermal expansion or contraction.

Tests were carried out in an air atmosphere, at four isothermal steps: 150°C, 160°C, 170°C, and 180°C. The relaxation profile for each temperature was monitored for 10^4 s, to allow for the complete observation of the long-term relaxation dynamics.

Arrhenius plot and activation energy (Ea) calculation

The temperature dependence of the relaxation process was quantitatively evaluated using the Arrhenius model. This approach allowed for the calculation of the *activation energy* (Ea), which represents the energy barrier that the dynamic covalent bonds must overcome to undergo exchange reactions and enable macroscopic flow.

For each isothermal stress-relaxation curve (from 150°C to 180°C), the characteristic *relaxation time* (τ*) was extracted. The relationship between the relaxation time and the *absolute temperature* (T) is described by the *Arrhenius equation* (Equation 5):

$$\tau(T) = \tau_0 * \exp\left(\frac{E_a}{RT}\right) \tag{5}$$

To determine Ea, Equation 5 was linearized, by taking the natural logarithm of both sides, obtaining Equation 6:

$$\ln(\tau) = \ln(\tau_0) + \frac{E_a}{R} * \frac{1}{T} \tag{6}$$

A linear regression was performed by plotting ln(τ) against the reciprocal of the absolute temperature (1/T, expressed in K^{-1}): this graphical representation is known as the *Arrhenius Plot*. From the resulting linear fit, the activation energy was derived from the *slope* (m) of the curve, according to the relation (Equation 7):

$$E_a = m * R \tag{7}$$

where R is the *universal gas constant* ($8.314\ \mathrm{J \cdot mol^{-1} \cdot K^{-1}}$).

The quality of the fit was assessed through the coefficient of determination (R^2), confirming the applicability of the Arrhenius model to the dynamic bond exchange mechanism within the investigated temperature range.

2.2.7 Differential scanning calorimetry (DSC) analysis

Differential scanning calorimetry (DSC) is a thermal analysis technique used to characterize the physical and chemical transitions of a material as a function of temperature and time. In the framework of vitrimer research, this analysis is essential to determine the *glass transition temperature* (Tg) range, identify potential post-curing phenomena (residual polymerization), and assess the thermal stability of the cross-linked network.

The DSC principle is based on measuring the difference in heat flow required to maintain a sample and a reference (typically an empty aluminum crucible) at the same temperature while both are subjected to a controlled heating or cooling program.

- When the sample undergoes an endothermic transition (such as glass transition or melting), it requires more heat than the reference to increase its temperature.
- When the sample undergoes an exothermic transition (such as crystallization or residual cross-linking reactions), it releases heat, requiring less energy from the heater.

The analysis yields a thermogram, plotting the heat flow (expressed in mW/mg) against temperature. These characteristic curves allow for the identification of several key features:

- *Glass transition temperature* (Tg) appears as a baseline shift (inflection point), corresponding to a change in the *specific heat capacity* (Cp) as the material transitions from a rigid glassy state to a rubbery state.
- *Exothermic peaks* indicate chemical reactions or crystallization processes. In photo-polymerized vitrimers, the absence of such peaks during the first heating scan confirms the successful conversion of the monomers.
- *Endothermic peaks* signify melting processes or the evaporation of volatile components.

In the present study, the 3D-printed vitrimer specimens were investigated using a *Netzsch DSC 214 Polyma system* (Selb, Germany – Figure 16). For each measurement, a sample of approximately 8-10 mg was placed in a 40 µl standard aluminum crucible and sealed with a pierced lid. An empty aluminum crucible was used as a reference.

FIGURE 16 - NETZSCH DSC 214 POLYMA (SELB, GERMANY)

All tests were conducted under a constant nitrogen purge at a flow rate of 40 ml/min to prevent any thermo-oxidative degradation during the scan. The following dynamic thermal cycle was applied to each sample:

1. *First heating scan*: from -60°C to 110°C at a constant rate of 10°C/min. This step was performed to erase the thermal history associated with the 3D printing process.
2. *Cooling scan*: from 110°C down to -60°C (10°C/min), to evaluate the crystallization behavior (if any) and re-establish the glassy state.
3. *Second heating scan*: from -60°C to 110°C (10°C/min).

The *glass transition region* was evaluated by analyzing the baseline shift in the second heating scan. The absence of exothermic peaks during the first heating scan was used as an indicator of the degree of curing achieved during the LCD photopolymerization process.

2.2.8 Dynamic-mechanical thermal analysis (DMTA)

Dynamic mechanical thermal analysis (DMTA) was employed to characterize the thermo-mechanical response of the synthesized vitrimers networks and determine their *glass transition temperature* (Tg). It is worth noting that the Tg determined via *dynamic-mechanical thermal analysis* (DMTA) may not perfectly coincide with the values obtained through *differential scanning calorimetry* (DSC). While both methodologies characterize the same thermal transition, the inherent differences in their detection principles (mechanical relaxation for DMTA versus caloric changes for DSC) can lead to slight discrepancies in the reported Tg.

DMTA analysis involves subjecting the sample to a sinusoidal stress or strain, monitoring the resulting viscoelastic response as a function of temperature. The primary parameters derived from DMTA are the *storage modulus* (E’), which represents the energy stored in the material, released after mechanical stress, and is a measure of the material's elasticity or stiffness; and the *loss modulus* (E”), which represents the energy dissipated as heat, reflecting the viscous nature of the material. Elastic characteristics prevail as long as the storage modulus remains higher than the loss modulus (E’ > E”); conversely, when the dissipative component becomes the major contributor, the material shifts to a predominantly viscous state (E’ < E”).

The ratio between loss modulus and storage modulus is referred to as *loss factor*, or tanδ, and indicates the degree of energy dissipation, quantifying the damping capability of the material. The peak of the tanδ curve is commonly used to identify the *glass transition temperature* (Tg), representing the transition from a rigid glassy state to a flexible rubbery state.

The analysis was performed on the *Anton Paar MCR 702e Multidrive* rheometer (Graz, Austria) equipped with a solid rectangular fixture (SRF), specifically configured for tensile testing (Figure 17). Rectangular samples with dimensions of 20 x 6 x 1 mm were mounted vertically and subjected to a sinusoidal oscillating tensile strain, with an amplitude of 0.01% at a fixed frequency of 1 Hz. The experimental protocol involved a temperature ramp from -70°C to 100°C with a constant heating rate of 3°C/min, allowing for a comprehensive assessment of the transition from the glassy to the rubbery state.

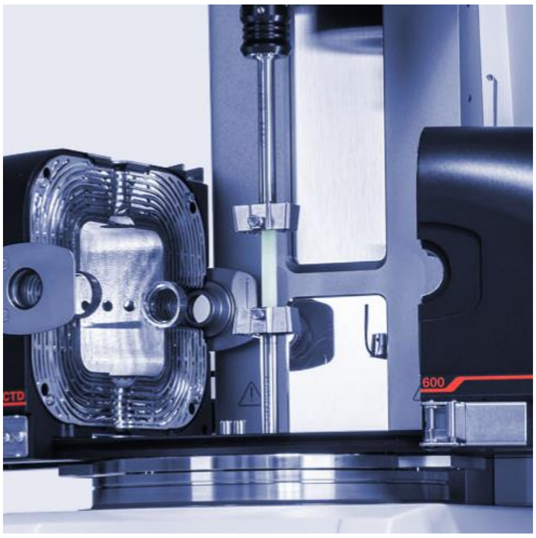

FIGURE 17 - ANTON PAAR MCR 702E MULTIDRIVE RHEOMETER (GRAZ, AUSTRIA) CONFIGURED FOR DMTA TENSILE TESTING

2.2.9 Self-healing experiment

The self-healing properties of the vitrimers were qualitatively evaluated through a scratch-repair test. The formulation “Gly/AESO:80-20” (80%wt glycerol, 20%wt AESO) was selected for testing, as it had previously exhibited excellent stress-relaxation capabilities (with a *relaxation time* (τ*) of 14.8 min at 180°C).

A sample, with dimensions of 20 x 6 x 1.5 mm, was damaged by a superficial scratch, manually inflicted using a cutter. Subsequently, the self-healing process was thermally activated by placing the sample on a hot plate at 180°C for a duration of 15 minutes.
The evolution of the scratch closure and the recovery of the surface integrity were monitored and recorded using a *Dino-Lite AM4815ZT* digital microscope (Figure 18), properly positioned. The device was equipped with a polarizing filter to minimize reflections and an optical magnification of up to 200x, allowing for a detailed observation of the interface disappearance and the material's flow into the damaged area.

FIGURE 18 - DINO-LITE AM4815ZT DIGITAL MICROSCOPE

2.2.10 Izod impact tests

The impact toughness of the 3D-printed specimens was evaluated through Izod impact tests performed at room temperature, using a *Zwick/Roell HIT25P* pendulum impact tester (Figure 20). The measurements were conducted in accordance with the ISO 180 standard to determine the energy absorbed by the material during sudden fracture. For this characterization, rectangular specimens, with dimensions of 55 x 12.7 x 3 mm, were 3D-printed in a notched configuration (Figure 19), to evaluate the material's sensitivity to stress concentrators.

FIGURE 19 - 3D PRINTED NOTCHED SAMPLES (GLY/AESO:60-40 FORMULATION) USED IN THE IZOD IMPACT TESTS

Each sample was clamped vertically in the instrument as a cantilever beam and struck by a calibrated pendulum. The energy dissipated during the fracture process was automatically recorded by the system and normalized by the residual cross-sectional area at the notch to calculate the *Izod impact strength* $[\mathrm{J/mm^2}]$. To ensure statistical reliability, at least four replicates were tested for each formulation, allowing for a quantitative comparison of the impact resistance and structural integrity of the different glycerol/AESO compositions.

FIGURE 20 - ZWICK/ROELL HIT25P PENDULUM IMPACT TESTER

2.2.11 Tensile tests

The quasi-static mechanical properties of the 3D-printed vitrimers were quantitatively evaluated through uniaxial tensile tests, in accordance with the ISO 527-2 standard. The measurements were performed at room temperature, using an *Instron 5966* universal testing machine (Figure 21), equipped with a 2 kN load cell and pneumatic grips. For this characterization, dog-bone shaped specimens (type 5A) were 3D-printed in accordance with the ISO 527-2 standard, ensuring a normalized geometry for the assessment of the material's mechanical response: gauge length of 26 mm, width of 4 mm, and thickness of 1.5 mm.

The samples were appropriately positioned between the grips and subjected to a constant deformation rate of 1 mm/min until failure occurred. The instrument recorded the force-extension data, which were subsequently processed to obtain engineering stress-strain curves. These curves allowed for the determination of the primary mechanical parameters, including the *Young's modulus* (E), calculated from the slope of the initial linear elastic region, the *tensile strength at break* (σ_{max}), and the *elongation at break* (ε_{b}). To ensure statistical reliability and reproducibility, at least five replicates were tested for each formulation, with results reported as average values and standard deviations. These parameters provided a quantitative comparison of the mechanical performance and ductility of the different glycerol/AESO compositions.

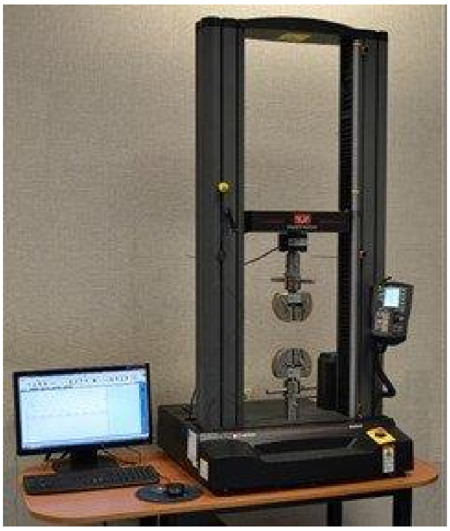

FIGURE 21 - INSTRON 5966 UNIVERSAL TESTING MACHINE

2.2.12 Reprocessing tests

The ability of the vitrimer networks to undergo structural recovery was evaluated by investigating the re-bonding of fractured specimens. The original dog-bone samples (ISO 527-2, type 5A), that had reached failure during the previous tensile tests, were utilized.

The two fractured parts of each specimen were carefully realigned and placed back into a metallic mold, ensuring intimate contact between the fracture surfaces. The reprocessing cycle was performed using a *Gibitre Instruments* heated hydraulic press (Figure 22) at a constant temperature of 180°C for a duration of 30 minutes, under an applied pressure of 200 bar.

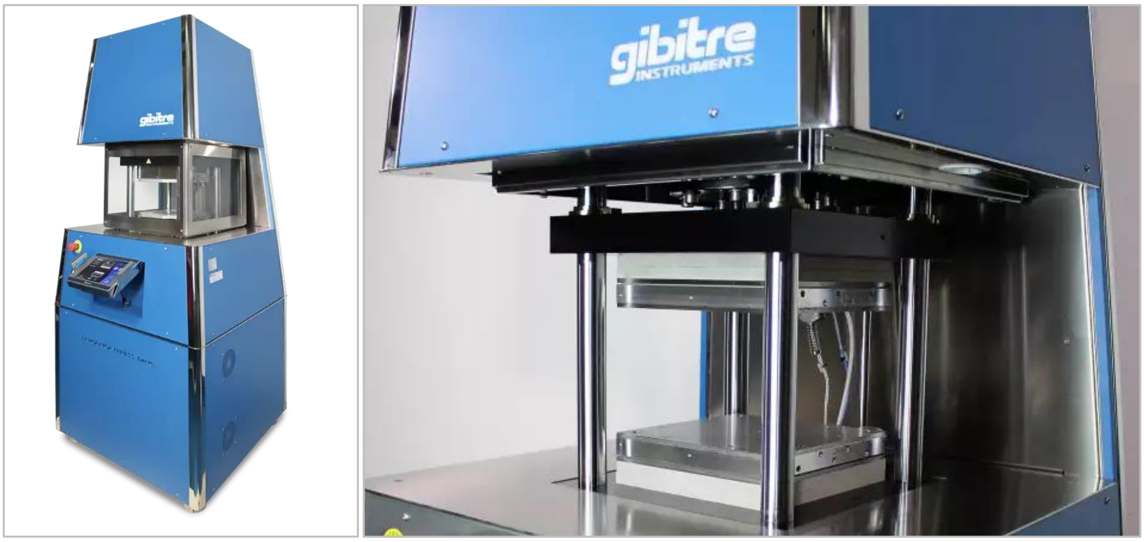

Figure 22 - Gibitre Instruments laboratory press-drive

This procedure was designed to trigger the transesterification-driven bond exchange reactions across the fracture interface, promoted by the simultaneous application of heat and pressure. After the thermal treatment, the specimens were cooled to room temperature under load to prevent thermal warping. The samples were then visually inspected to confirm the successful welding of the fragments into a single, cohesive body.

3. Results and discussion

This chapter presents and evaluates the experimental results obtained from the printing tests, as well as the characterization of the photocurable resins and their corresponding 3D-printed vitrimers.

The discussion is structured to provide a comprehensive overview of the material's behavior, beginning with the analysis of the physico-chemical properties of the liquid formulations, to characterize their rheological profile and reactivity. This is followed by a printability assessment aimed at defining the optimal processing parameters for the 3D printing stage. Finally, the thermal and mechanical performance of the cured vitrimeric networks is discussed, with a specific focus on the effectiveness of the associative bond-exchange mechanisms.

By correlating the processing conditions with the final material properties, this analysis aims to validate the potential of these dynamic networks for sustainable additive manufacturing.

3.1 Rheological assessment and photocuring kinetics of the resin formulations

3.1.1 Viscosity analysis

The viscosity of the photocurable formulations was evaluated as a function of the shear rate to determine their suitability for the vat photopolymerization process. As shown in Figure 23, the rheological behavior is strongly influenced by the ratio between glycerol and AESO.

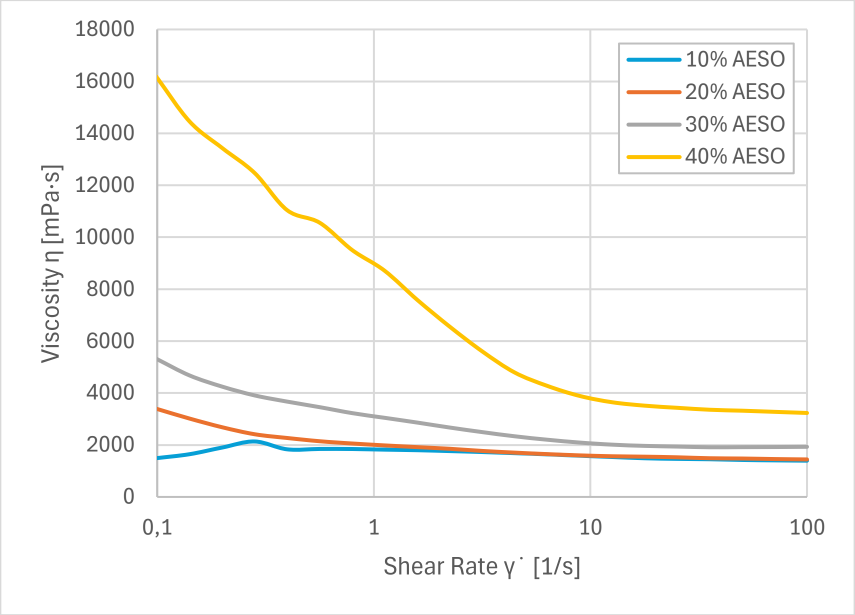

FIGURE 23 - COMPARISON OF SHEAR RATE-VISCOSITY CURVES FOR THE DIFFERENT FORMULATIONS

A clear upward trend in viscosity is observed as the AESO concentration increases from 10% to 40%. The formulation with 40% AESO exhibits the highest initial viscosity, exceeding 16000

mPa·s at low shear rates, whereas the 10% AESO formulation remains significantly lower, around 1500–2000 mPa·s.
All formulations, particularly those with higher AESO content (30% and 40%), exhibit shear-thinning (pseudoplastic) behavior. This is evidenced by the marked decrease in viscosity as the shear rate increases from 0.1 to 100 1/s. This phenomenon is typical of long-chain monomers like AESO, which tend to orient themselves along the flow direction under stress.
The minor instability observed for the 10% AESO sample at shear rates below 0.5 1/s is likely due to the instrument approaching its lower torque resolution limit, given the significantly lower viscosity of this formulation compared to the AESO-rich blends.

In vat-based technologies (LCD/DLP), low viscosities, typically between 200 and 1500 mPa·s, are generally preferred to facilitate the recoating process and ensure a uniform resin layer. [28] In contrast, certain of the bio-derived formulations examined in this study operate within a higher viscosity range, extending beyond standard commercial specifications. As reported in Table 2, the formulations containing 10% to 30% AESO exhibit plateau viscosities between 1395 and 1930 mPa·s; however, such values are well-documented for high-performance functional and shape-memory resins. [45, 46] Although elevated viscosity can hinder resin reflow, these systems can be accurately processed by optimizing the “rest-time” before UV exposure, ensuring precise layer formation even as values approach 2000 mPa·s. [46] This strategy enables the incorporation of high-molecular-weight bio-precursors like AESO, which are fundamental to achieving the target thermo-mechanical properties of the final vitrimer. [47] Accordingly, even the 40% AESO formulation, with a viscosity exceeding 3200 mPa·s, was successfully printed and characterized, despite requiring a strategic increase in the build-plate delay to allow for proper material leveling between successive layers.

TABLE 2 – PLATEAU SHEAR RATE VISCOSITY (η) VALUES AT 25°C

Formulation	Viscosity [mPa·s]
Gly/**AESO**:90-**10**	1395
Gly/**AESO**:80-**20**	1444
Gly/**AESO**:70-**30**	1930
Gly/**AESO**:60-**40**	3233

3.1.2 Real-time photorheology analysis

The time-dependent evolution of the *storage modulus* (G’) for each formulation is presented in Figure 24A. A significant correlation is observed between the AESO content and the final plateau of the *storage modulus*: increasing the AESO concentration from 10% to 40% led to a progressive and substantial increase in G’. The 40% AESO formulation reached a plateau near $1.95 \cdot 10^6$ Pa, whereas the 10% AESO formulation yielded a significantly lower value, approximately $1 \cdot 10^5$ Pa ($2.36 \cdot 10^5$ Pa for the 20% AESO formulation and $7.95 \cdot 10^5$ Pa for the 30% AESO one). Upon UV exposure (starting at 30 s), all samples exhibited an immediate response, with the curing rate, indicated by the slope of the curves, increasing proportionally with the soybean oil content. The formulation with 40% AESO exhibited the steepest slope, suggesting a faster rate of network formation. This could be attributed to the higher functionality of the AESO molecules, which provides more reactive sites per chain, thus accelerating the attainment of a high cross-linking density.

All curves reached a stable plateau within 150 seconds of the total test time (approximately 120 seconds of irradiation), indicating that the photopolymerization reached full conversion under the tested conditions.

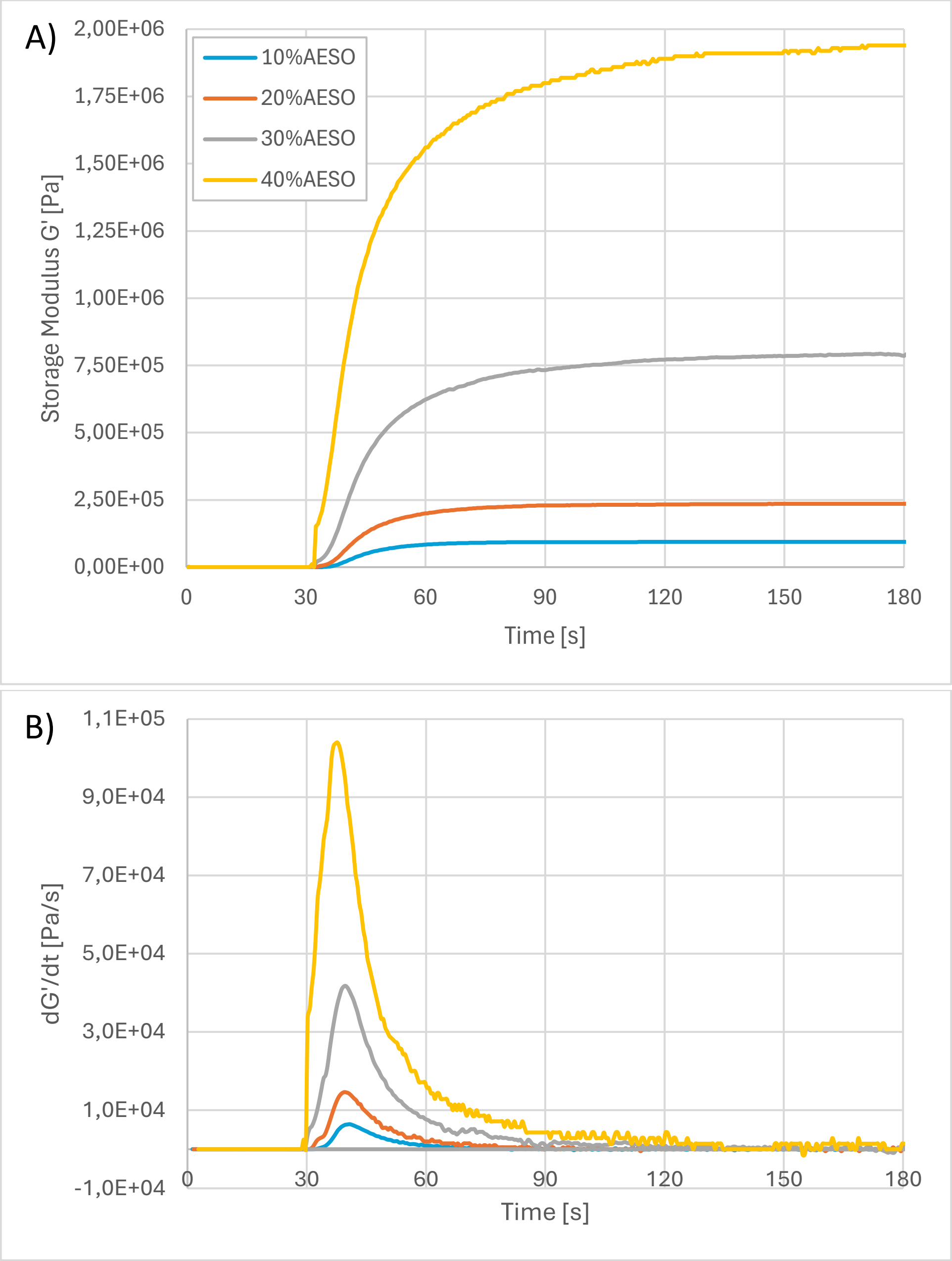

FIGURE 24 - STORAGE MODULUS G’ CURVES (A) AND THEIR FIRST DERIVATIVE WITH RESPECT TO TIME (B)

To further investigate the curing kinetics, the first derivative of the storage modulus with respect to time (dG’/dt) was calculated (Figure 24B). This analysis provides a direct measurement of the polymerization rate and allows for the identification of the point of maximum reactivity. The slope of the derivative curve represents the polymerization rate, while its peak identifies the point at which this rate reaches its maximum value.

As shown in Figure 24B, the steepness of the derivative curves increases with the AESO concentration in the formulation; similarly, the peaks become higher and slightly shifted toward shorter times as the percentage of AESO increases. This confirms that increasing the soybean oil content not only leads to a stiffer final network, as evidenced by the G’ curves, but also significantly accelerates the curing kinetics upon UV activation.

Interestingly, the return to the baseline for the derivative curves, after reaching their peaks, is more protracted in formulations with higher AESO concentrations. This suggests that, despite the higher initial reactivity, the rapid buildup of a dense and stiff cross-linked structure (as evidenced by the high G’ plateau) leads to diffusion-limited kinetics. [48] In this regime, the mobility of the remaining reactive species is restricted, resulting in a prolonged stabilization phase before the reaction rate effectively reaches zero. [49, 50]

The efficiency of the photopolymerization process is further highlighted by the *gel point* values, defined as the time at which the crossover between G’ and G” occurs. As shown in Table 3, as the AESO content increases, a reduction in gelation time is observed.

TABLE 3 - GELATION TIMES (GEL POINTS)

Formulation	**Gel point [s]**
Gly/**AESO**:90-**10**	3
Gly/**AESO**:80-**20**	1.5
Gly/**AESO**:70-**30**	1
Gly/**AESO**:60-**40**	0.5

The gelation time drops from 3.0 s for the 10% AESO sample to a mere 0.5 s for the 40% AESO one. This six-fold acceleration confirms that the higher functionality of the bio-based cross-linker ensures an almost instantaneous transition to a solid network upon UV exposure. Such rapid gelation is highly desirable for high-resolution 3D printing, as it minimizes resin flow and vat-edge curing during the layer-by-layer assembly.

3.2 LCD 3D printing

3.2.1 Jacob’s working curves and 3D printing parameters optimization

To evaluate the 3D printing parameters for each formulation, the curing behavior was characterized using *Jacob’s working curve* model. By measuring the *cure depth* (Cd) as a function of the *irradiation energy* (E), two fundamental parameters were determined: the *critical exposure* (Ec), representing the minimum energy required to initiate gelation, and the *penetration depth* (Dp), which indicates the sensitivity of the resin to light attenuation.

The experimental data for the four formulations (10%, 20%, 30%, and 40% AESO) were plotted, and the linear regression of Cd vs. ln(E) is provided in Figure 25.

The curves reveal a clear correlation between the AESO content and the resin's optical printing parameters. The *penetration depth* (Dp) shows a steady decrease from 1029 µm (10% AESO) to 837 µm (40% AESO). This reduction indicates that higher concentrations of soybean oil confine the UV light more effectively, which is a positive trait for improving Z-axis resolution and reducing over-curing.

Simultaneously, the *critical exposure* (Ec) slightly increases with the AESO content, reaching a plateau at 33 mJ/cm^2 for the 30% and 40% AESO formulations. This slight increase in Ec indicates that, although the AESO accelerates the reaction once triggered (as observed in the real-time photorheology analysis), the system requires a marginally higher initial energy threshold to initiate the stable polymerization of a solid layer, compared to the glycerol-richer samples.

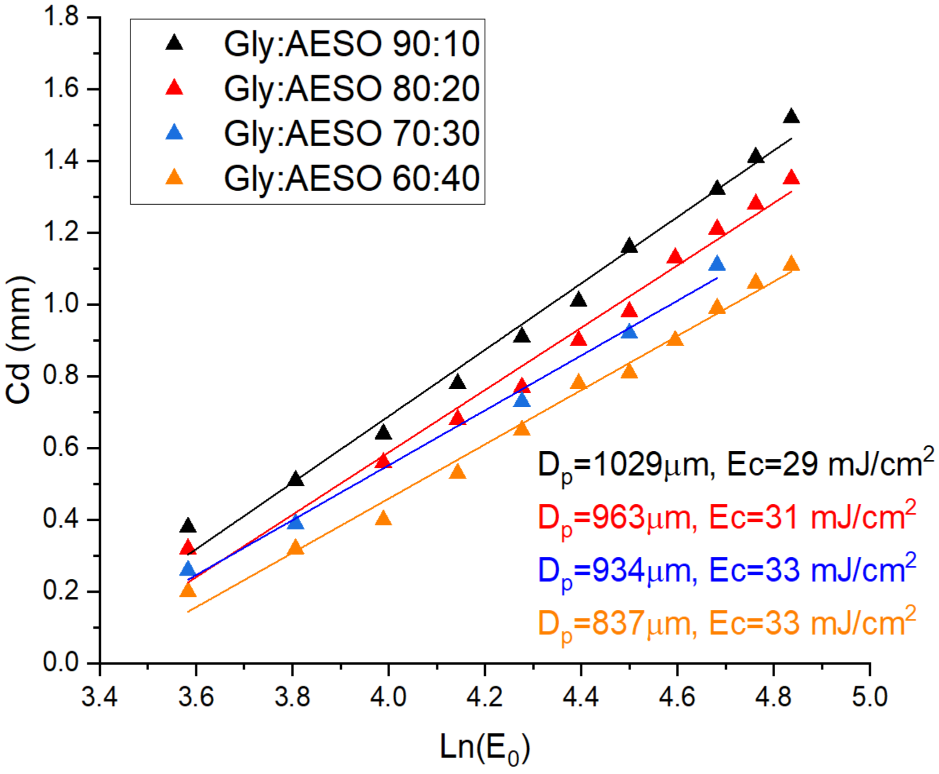

FIGURE 25 - JACOB'S WORKING CURVES WITH THE VALUES OF PENETRATION DEPTH (DP) AND CRITICAL EXPOSURE (EC) FOR THE RESIN FORMULATIONS

Based on these findings, the slightly higher *critical exposure* (Ec) observed for the 30% and 40% AESO specimens necessitated a careful optimization of the initial layer *exposure times* (t_{exp}). Specifically, to ensure robust adhesion to the building platform and to overcome the higher energy threshold for stable gelation, the *exposure time* for the bottom layers was increased proportionally to the AESO content. This adjustment effectively compensated for the initial resistance to network formation, preventing delamination and ensuring a successful printing process for all tested ratios.

TABLE 4 - OPTIMAL EXPOSURE TIMES FOR A LAYER THICKNESS OF 100 µM

Formulation	**Opt. t_{exp} [s]**
Gly/**AESO**:90-**10**	18.1
Gly/**AESO**:80-**20**	19.4
Gly/**AESO**:70-**30**	20.6
Gly/**AESO**:60-**40**	20.9

The optimal *exposure times* (t_{exp}) for a *layer thickness* of 100 µm (Table 4) were determined via Equation 8, which correlates *critical exposure* (Ec), *penetration depth* (Dp) and *light intensity* (I), based on *Jacob's working curve model*:

$$t_{exp} = \frac{E_c}{I} * \exp\left(\frac{C_d}{D_p}\right) \qquad (8)$$

The required exposure time increases with the AESO concentration, ranging from 18.1 s (10% AESO) to 20.9 s (40% AESO). This trend can be attributed to the interplay between the resins' optical properties and their critical energy thresholds. As previously discussed, the *penetration depth* (Dp) decreases as the AESO content rises, meaning the UV light is more strongly attenuated as it travels through the resin. Consequently, a longer *exposure time* (t_{exp}) is necessary to ensure that the light reaches sufficient depth to photo-cure a full 100 µm layer. Furthermore, the slightly higher *critical exposure* (Ec) for the AESO-richer formulations contributes to this increase, as more energy is required to initiate the stable formation of a solid network.

3.2.2 3D printing of complex geometries

To further validate the printability of the bio-based formulations, a series of hollow spheres with intricate surface patterns were fabricated. These geometries were selected to assess the resin's ability to maintain structural integrity in thin-walled sections and to evaluate the resolution limits across different scales.

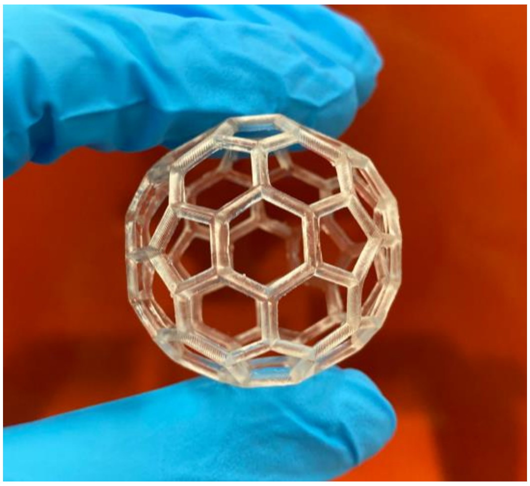

FIGURE 26 - HOLLOW SPHERE WITH HEXAGONAL PATTERN (350 LAYERS - GLY/AESO:70-30)

The printing process focused on the two intermediate formulations, with glycerol/AESO ratios of 80/20 and 70/30, which represented the best balance between viscosity, reactivity and penetration depth. Using a *layer thickness* of 100 µm and the optimized *exposure times* derived from *Jacob's working curves* (19.4 s and 20.6 s, respectively), the following results were observed:

- *Scalability*: The resins successfully reproduced the complex patterns across a wide range of dimensions, from larger spheres with a diameter of 3.5 cm down to miniaturized versions with a diameter of less than 1.5 cm.

- *Geometric fidelity*: Even at the smallest scale, the hollow nature of the spheres was preserved without internal clogging. This confirms that the *penetration depth* (Dp) was sufficiently controlled, to prevent unwanted polymerization of the liquid resin trapped inside the cavity during the layer-by-layer assembly.
- *Structural stability*: The thin struts of the patterns showed no signs of collapsing or warping, indicating that the cross-linking density, achieved with the optimized exposure parameters, was sufficient to support the overhanging features of the spherical geometry.

Following the printing process, a standardized washing procedure in isopropanol was performed. The moderate viscosity of the blends, even at 30% AESO concentration, allowed for the efficient removal of the unreacted liquid formulation from the internal voids and fine meshwork, ensuring the final parts maintained their designed porosity.

Representative photographs of the 3D printed spheres are shown below (Figure 26 – 36), ranging from the largest to the smallest prototypes, highlighting the geometric accuracy of the lattice structures.

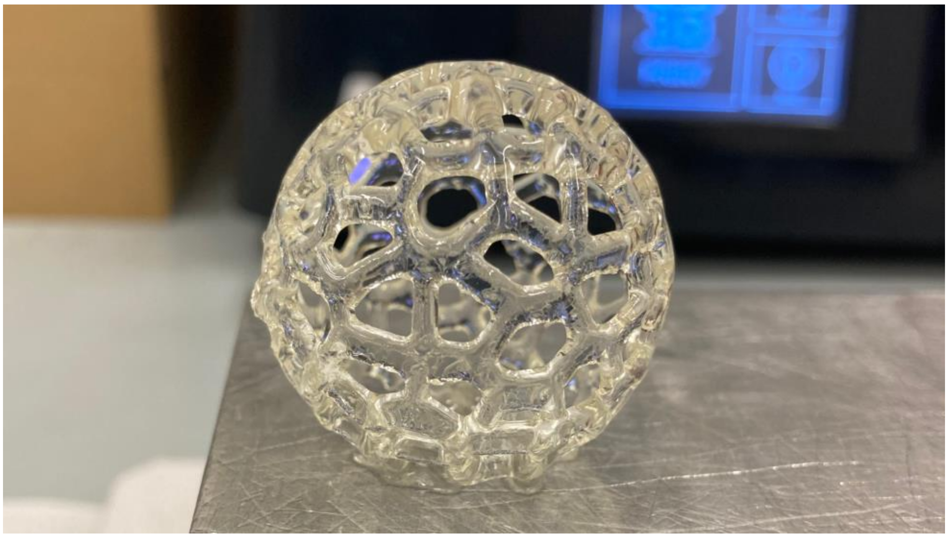

FIGURE 27 - HOLLOW SPHERE WITH *VORONOI* PATTERN (350 LAYERS - GLY/AESO:80-20)

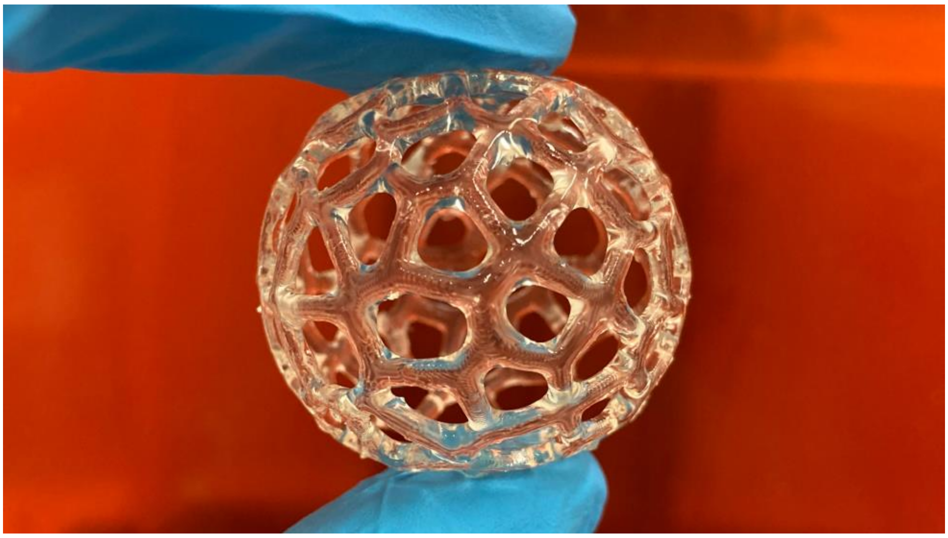

FIGURE 28 - HOLLOW SPHERE WITH *VORONOI* PATTERN (350 LAYERS - GLY/AESO:80-20)

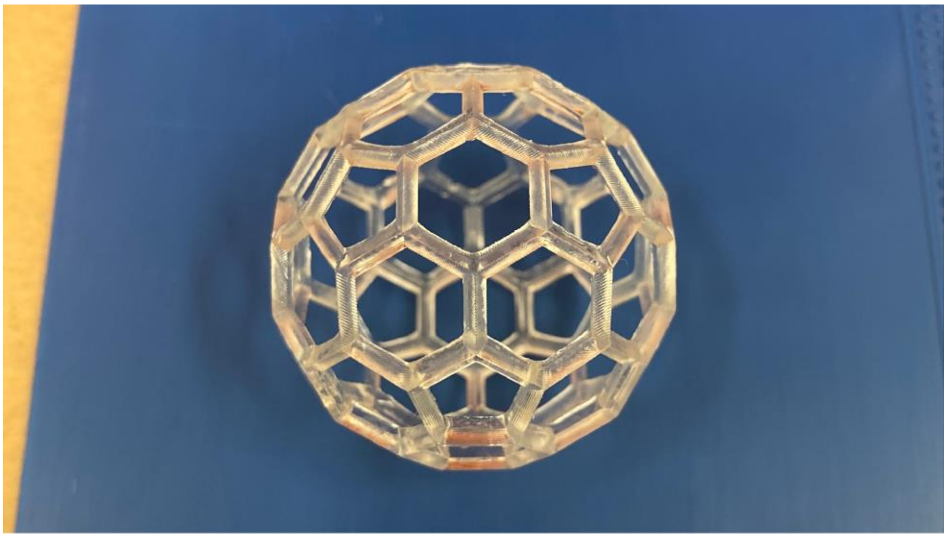

Figure 29 - Hollow sphere with hexagonal pattern (350 layers - Gly/AESO:70-30)

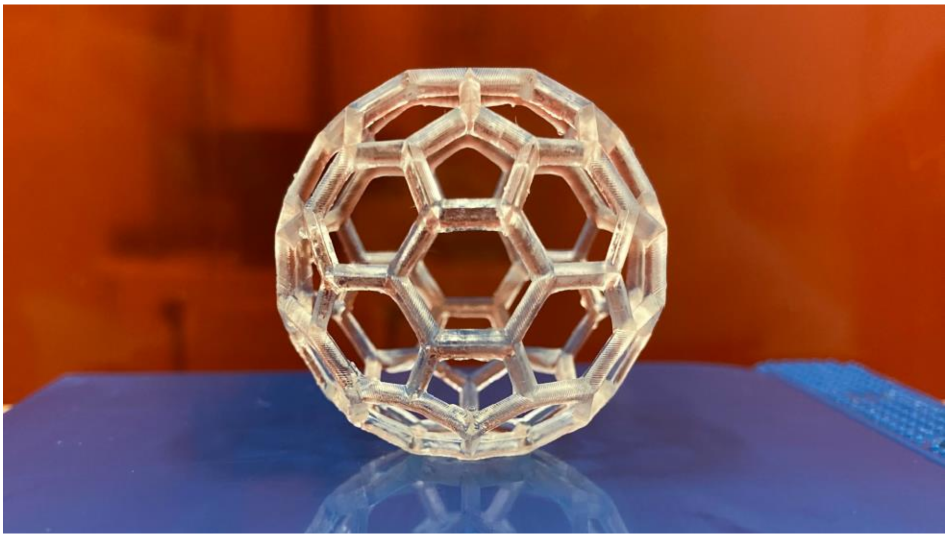

Figure 30 - Hollow sphere with hexagonal pattern (350 layers - Gly/AESO:70-30)

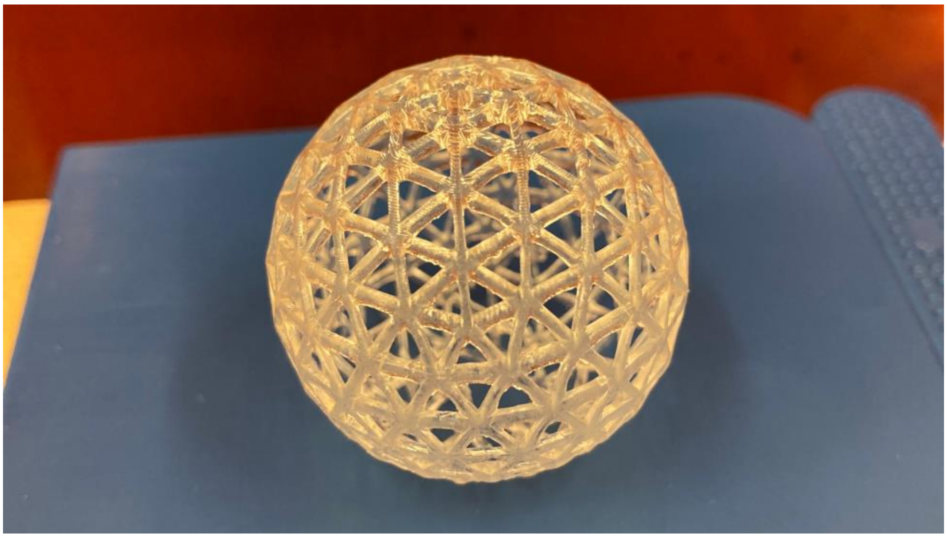

Figure 31 - Hollow sphere with *geodesic* pattern (350 layers - Gly/AESO:70-30)

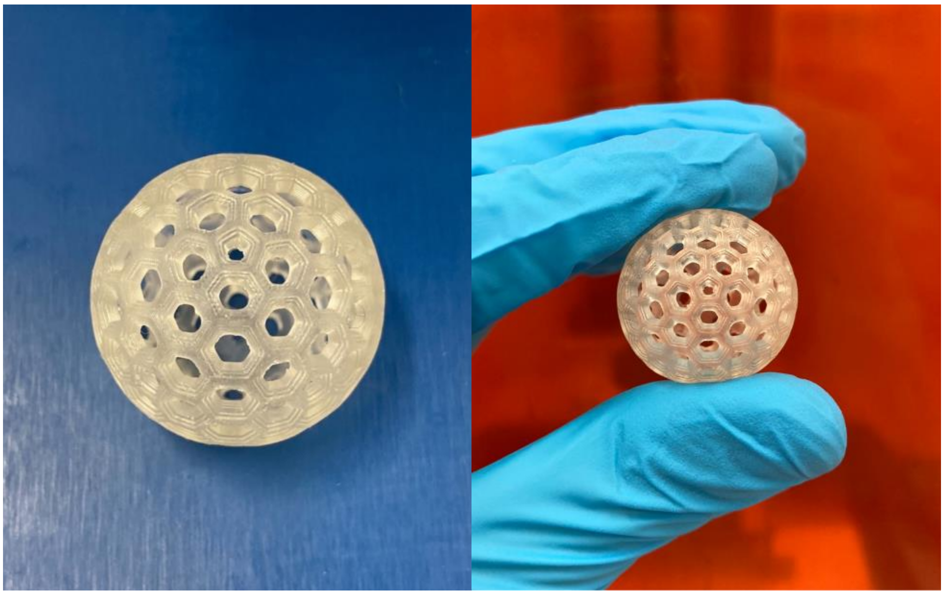

Figure 32 - Hollow spheres with hexagonal pattern (250 layers - Gly/AESO:70-30)

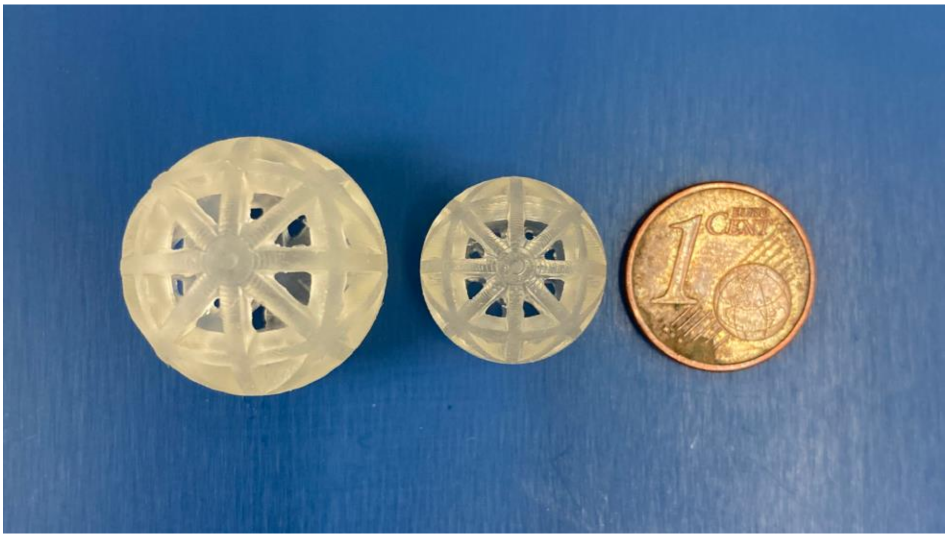

Figure 33 - Hollow spheres with triangular pattern (200 & 150 layers - Gly/AESO:80-20)

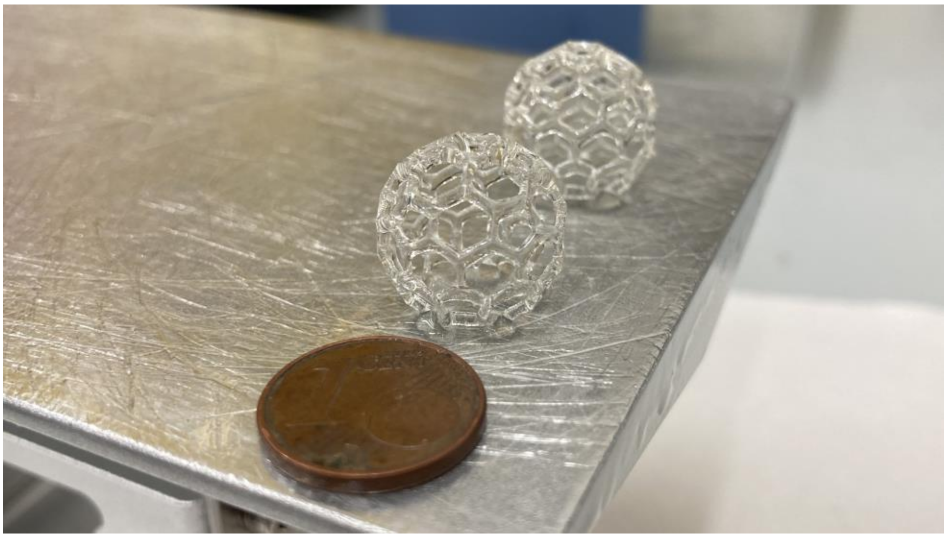

Figure 34 - Hollow spheres with hexagonal pattern (150 layers - Gly/AESO:70-30)

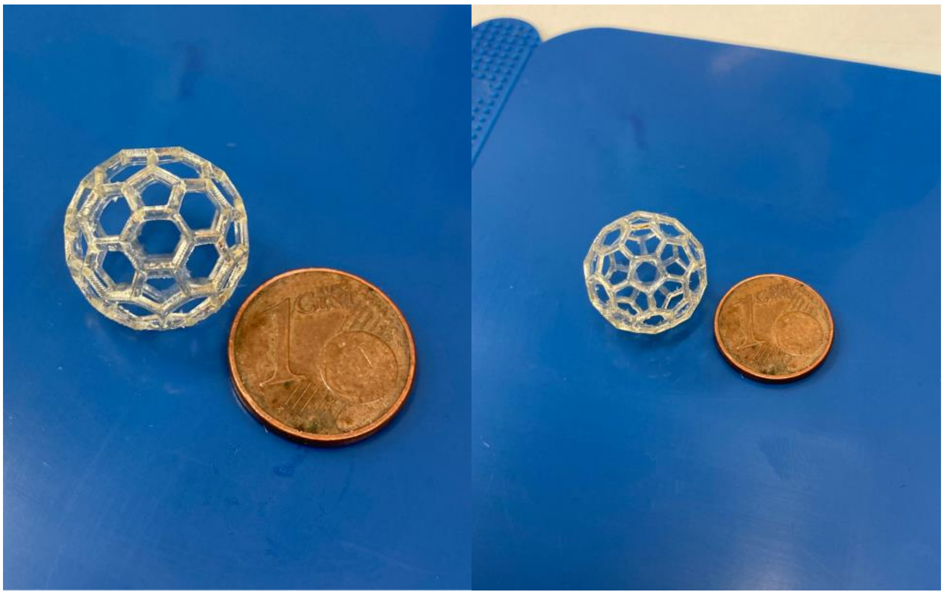

Figure 35 - Hollow spheres with hexagonal pattern (150 layers - Gly/AESO:70-30)

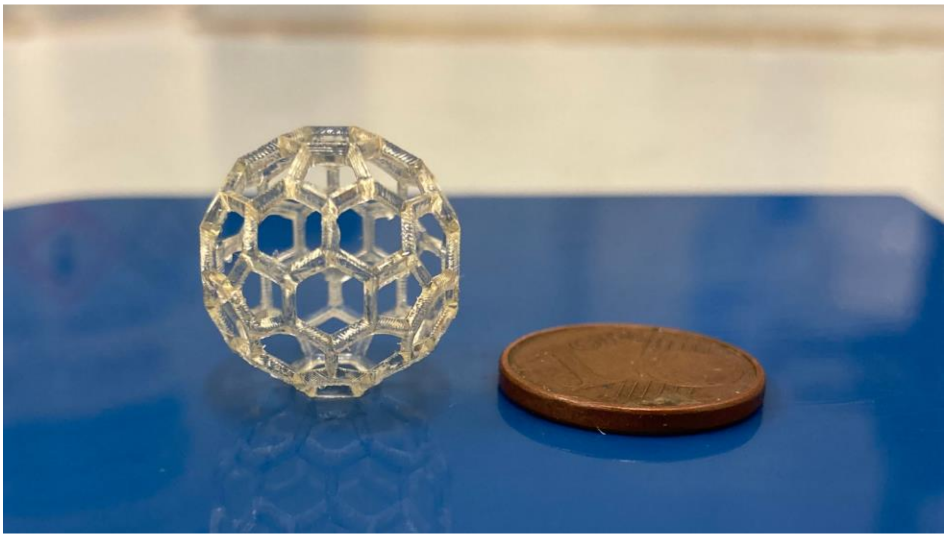

Figure 36 - Hollow sphere with hexagonal pattern (145 layers - Gly/AESO:70-30)

Overall, both tested resin systems proved capable of supporting intricate features and thin-walled patterns without compromising geometric fidelity. Even the formulation containing 30% soybean oil, which presented a higher viscosity, was processed successfully, confirming that the printing parameters were sufficiently optimized to overcome the rheological challenges of the bio-sourced components.

3.3 FTIR spectroscopic analysis and *degree of conversion* (DC)

The chemical structural changes occurring during the UV-curing process were monitored via FTIR spectroscopy. This analysis is crucial to verify the consumption of reactive functional groups and to quantify the efficiency of the photopolymerization process for the different bio-based formulations.

The *degree of conversion* (DC) was quantitatively evaluated by monitoring the absorbance peak at 1635 cm⁻¹, corresponding to the C=C stretching vibration of the acrylate groups. The results, summarized in Table 5, reveal a high level of conversion across all formulations, exceeding 87% in all cases.

TABLE 5 - DEGREES OF CONVERSION (DC) DETERMINED VIA COMPARISON OF THE PEAK AREAS AT 1635 CM⁻¹

Formulation	**Degree of conversion (DC)**
Gly/**AESO**:90-**10**	87.16 %
Gly/**AESO**:80-**20**	87.85 %
Gly/**AESO**:70-**30**	88.36 %
Gly/**AESO**:60-**40**	88.65 %

The FTIR spectra, before (*pre*) and after (*post*) photopolymerization, are reported below for each formulation. The inset (top left) shows the detail of the peaks in the 1635 cm⁻¹ region (C=C stretching), whose areas were used for the calculation of the *degree of conversion* (DC).

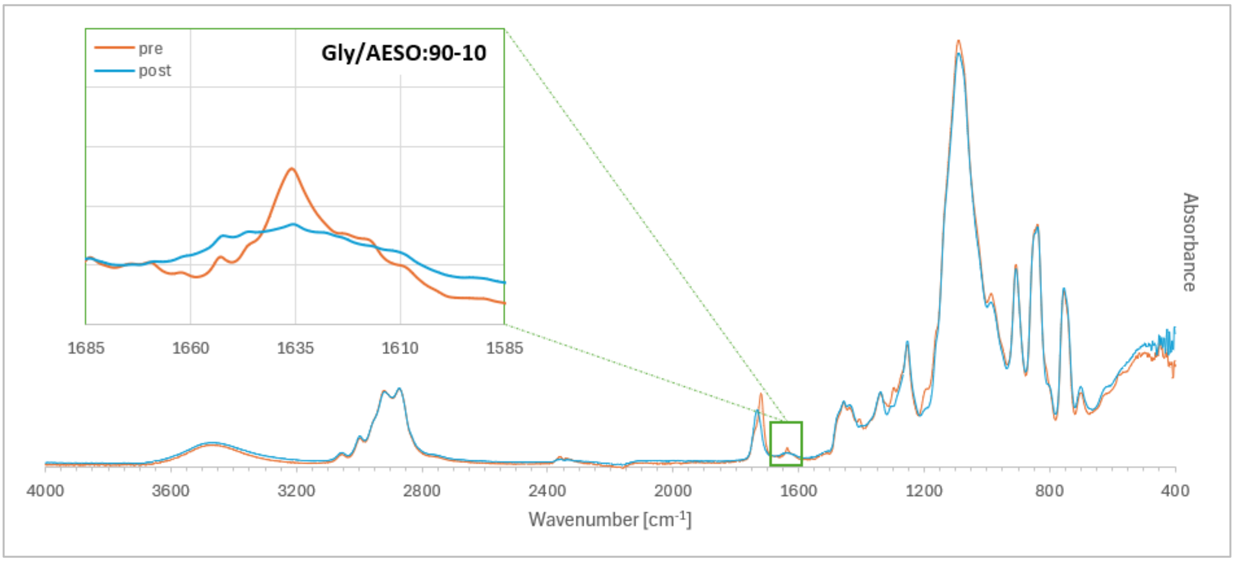

FIGURE 37 - GLY/AESO:90-10 FTIR SPECTRA BEFORE AND AFTER 3D PRINTING

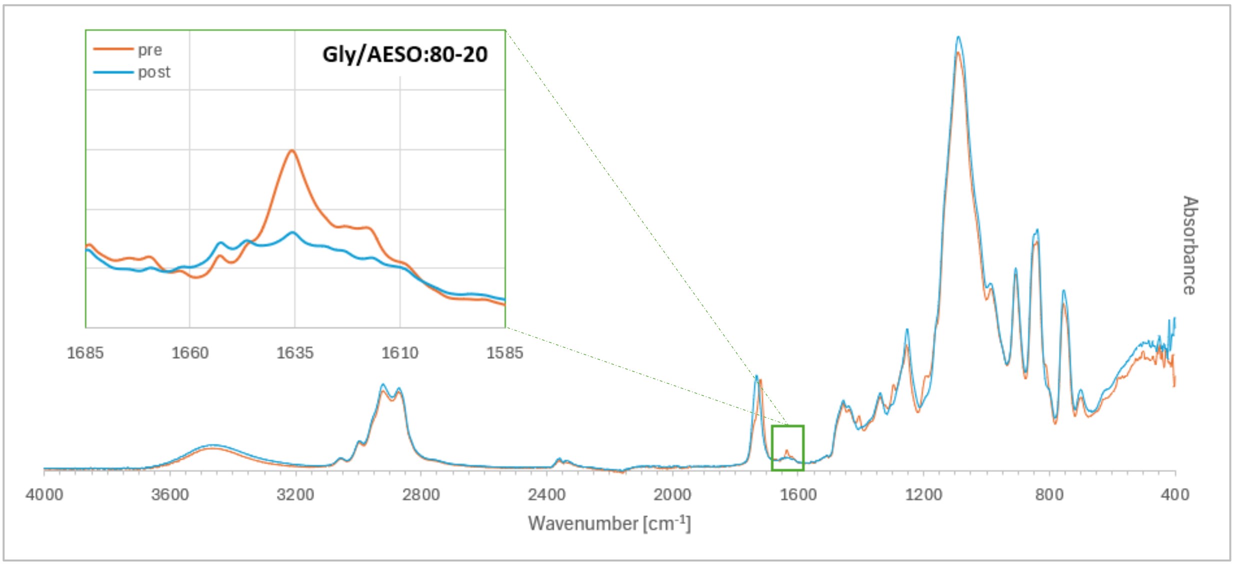

FIGURE 38 - GLY/AESO:80-20 FTIR SPECTRA BEFORE AND AFTER 3D PRINTING

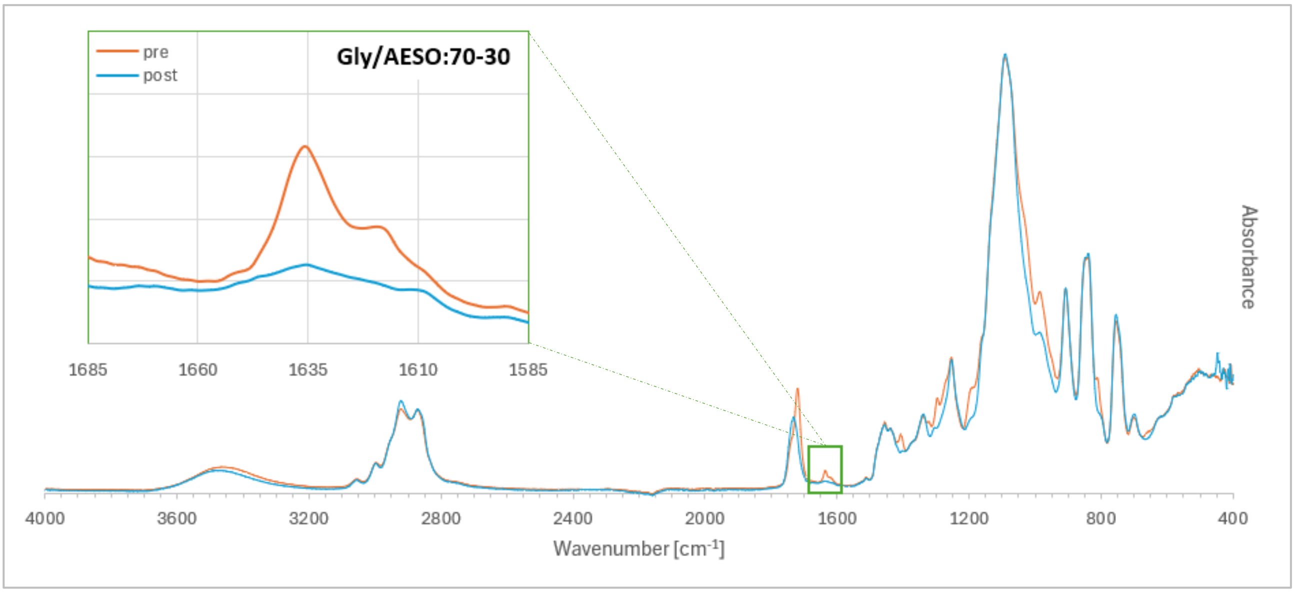

FIGURE 39 - GLY/AESO:70-30 FTIR SPECTRA BEFORE AND AFTER 3D PRINTING

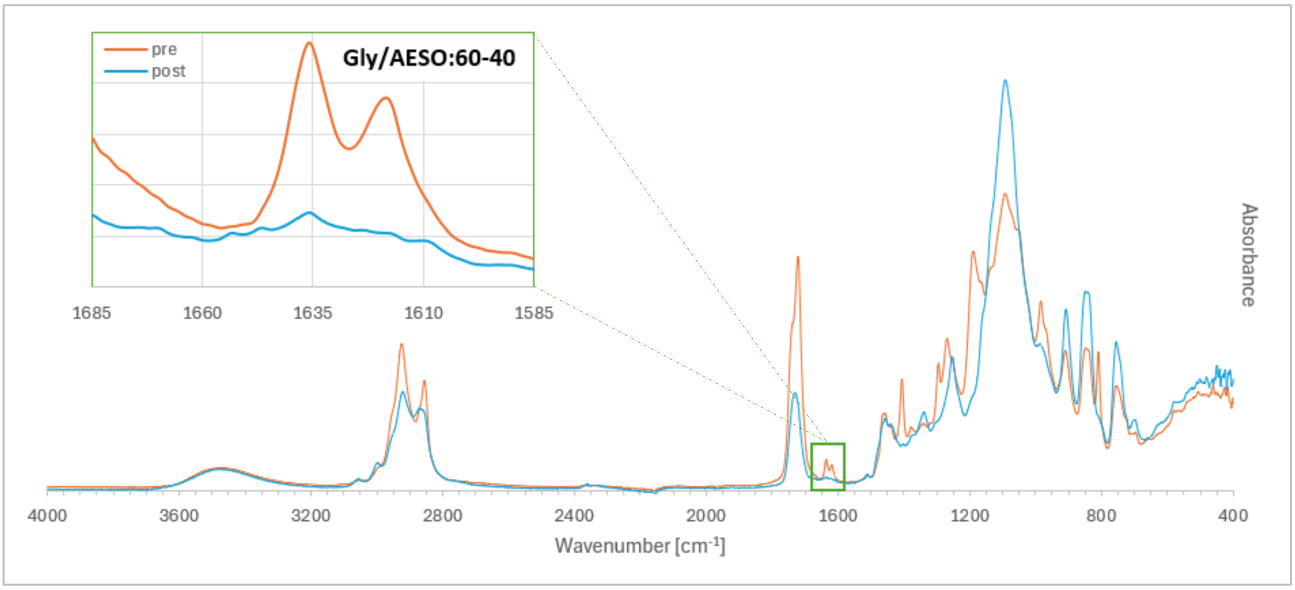

FIGURE 40 - GLY/AESO:60-40 FTIR SPECTRA BEFORE AND AFTER 3D PRINTING

The FTIR analysis confirms the high reactivity of all tested systems, which achieved conversion levels near the theoretical limit for densely cross-linked networks. This result is particularly significant considering that in such systems, molecular mobility typically becomes restricted as the resin undergoes vitrification during the UV-curing process. [39, 40] Interestingly, the data reveal a slight but consistent increase in the degree of conversion (from 87.16% to 88.65%) as the AESO content rises, suggesting that the multi-functional nature of the soybean oil facilitates a more efficient integration into the polymer matrix. Despite the higher viscosity of the 40% AESO formulation, the flexible fatty acid chains act as "internal spacers", maintaining sufficient chain mobility during exposure to allow for an exhaustive reaction of the vinyl groups. [41]

3.4 Stress-relaxation dynamics and *activation energy* (Ea)

The dynamic nature of the synthesized polymer networks, governed by associative bond-exchange reactions, was investigated through systematic stress-relaxation experiments. These tests, conducted within a temperature range of 150–180°C, aimed to elucidate the influence of the chemical architecture on the *relaxation time* (τ*) and the overall *activation energy* (Ea) required for the transesterification-driven topology rearrangement.

A preliminary phase of this study involved assessing the efficacy of the Miramar A99 catalyst in triggering the vitrimeric response. To decouple the effects of the polymer matrix from the catalytic action, the 80% glycerol - 20% AESO formulation (Gly/AESO:80-20) was employed as a benchmark and evaluated at three distinct loading levels of Miramar A99 catalyst: 0, 2.5 and 5 phr. The experimental curves, obtained for these three 20% AESO samples (*0A99, 2.5A99* and *5A99*) are reported below (Figure 41 – 42).

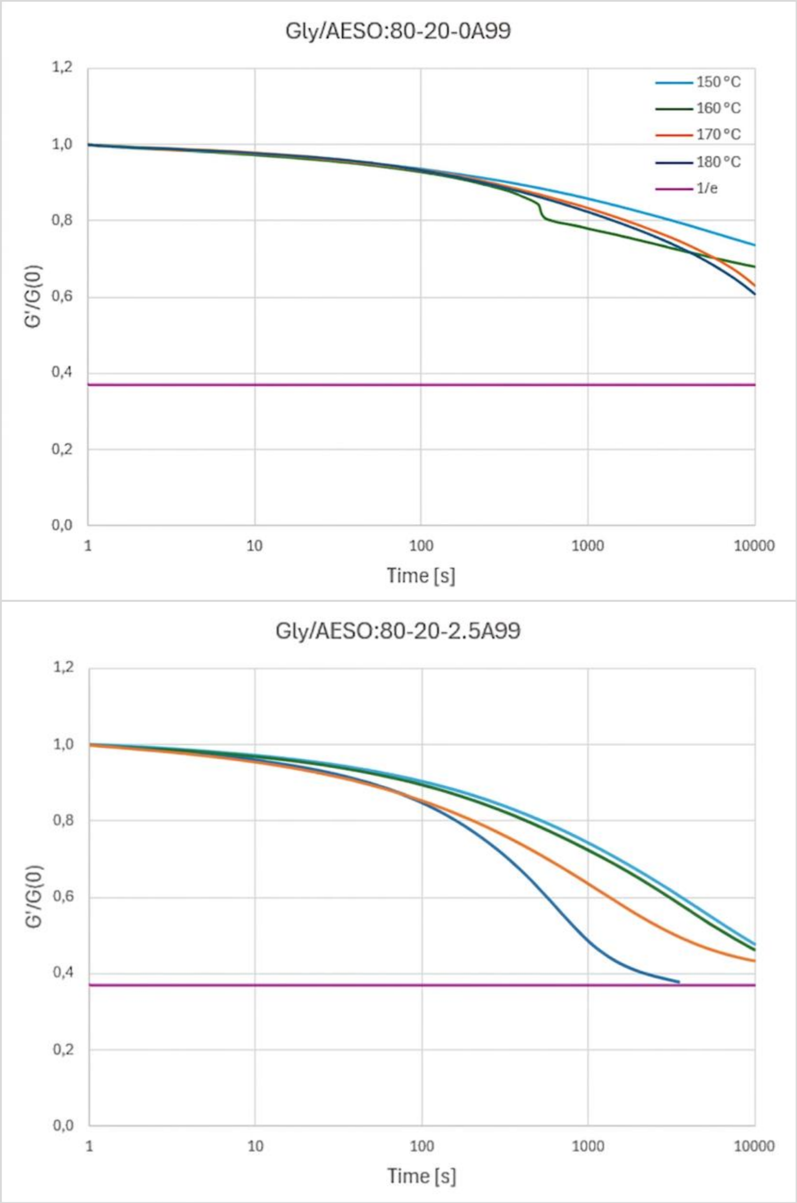

Figure 41 - Effect of Miramar A99 catalyst loading (0 and 2.5 phr) on the stress-relaxation behavior of the Gly/AESO-80:20 network in the temperature range 150-180°C

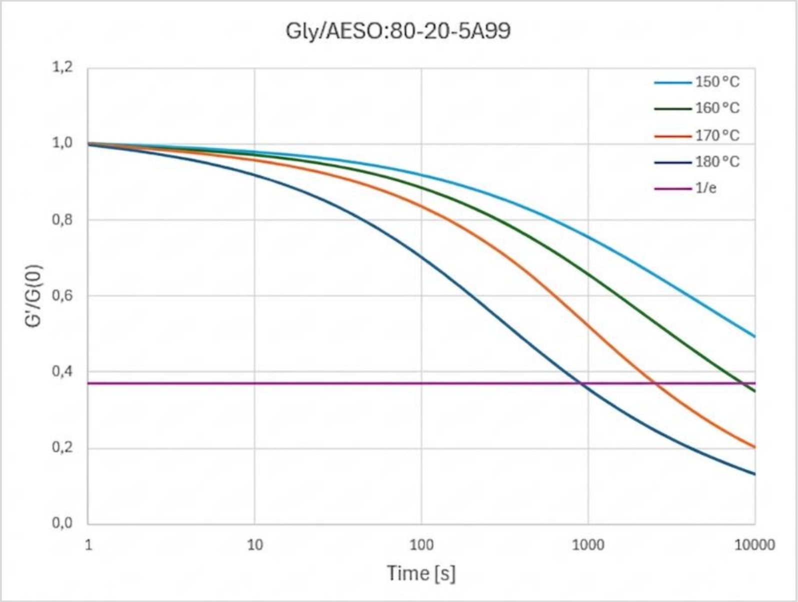

FIGURE 42 - STRESS-RELAXATION PROFILES FOR THE 80/20 RESIN SYSTEM WITH STANDARDIZED 5 PHR OF MIRAMAR A99 CATALYST, ILLUSTRATING THE ACCELERATED BOND-EXCHANGE KINETICS AT HIGHER TEMPERATURES

The experimental data clearly highlight the catalyst's indispensable role. While the uncatalyzed (*0A99*) and low-loading (*2.5A99*) variants exhibited negligible or incomplete stress dissipation, the formulation containing 5 phr of Miramar A99 achieved a comprehensive relaxation profile within the observation window. This behavior suggests that a critical threshold of catalytic sites is required to lower the kinetic barrier of transesterification, thereby enabling the macroscopic flow of the cross-linked network. Consequently, this concentration, which had been initially selected based on existing literature, was standardized for all subsequent formulations and, as a result, these systems were not tested at catalyst loadings below 5 phr. The temperature-dependent stress-relaxation profiles, obtained for the 10%, 30% and 40% AESO samples are reported below (Figure 43 – 44 – 45).

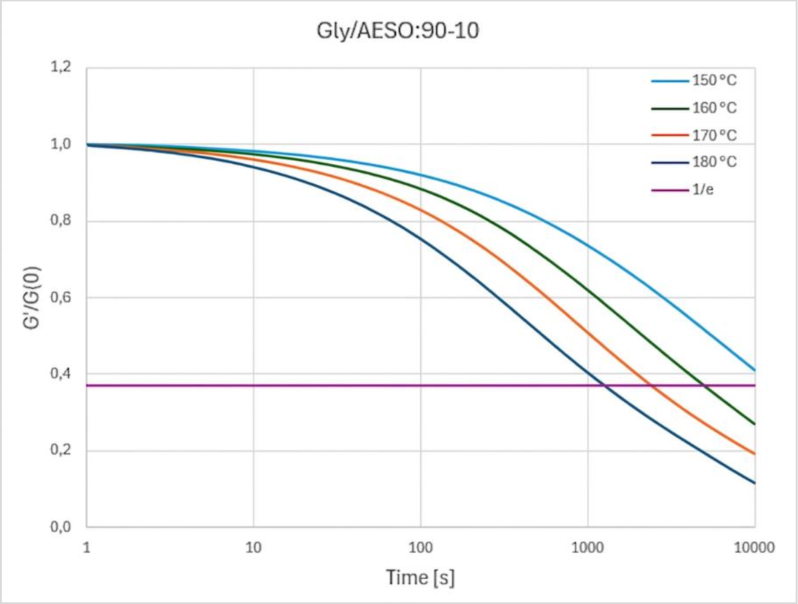

FIGURE 43 - GLY/AESO:90-10 STRESS-RELAXATION CURVES (150-180°C)

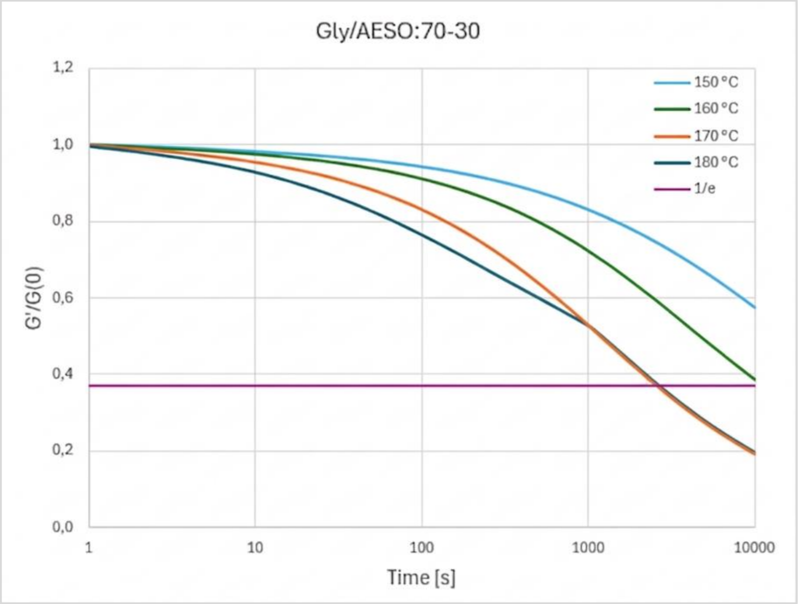

FIGURE 44 - GLY/AESO:70-30 STRESS-RELAXATION CURVES (150-180°C)

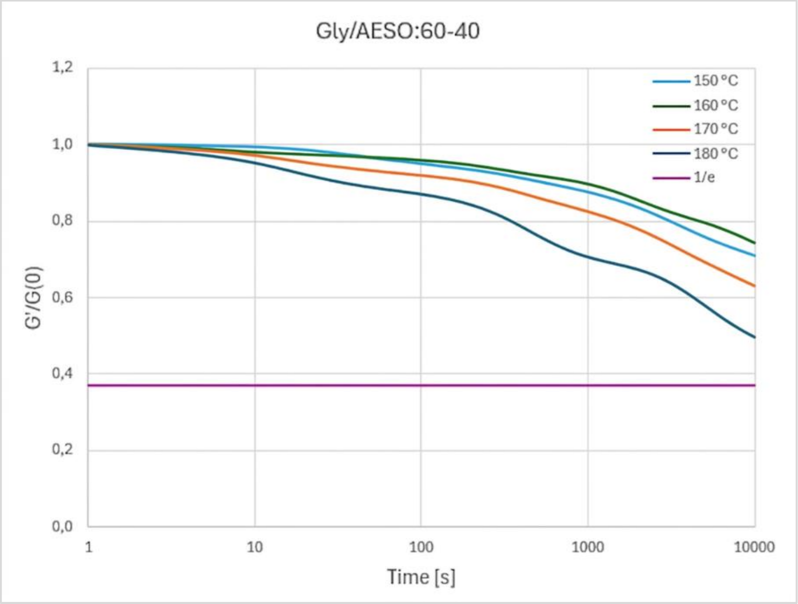

FIGURE 45 - GLY/AESO:60-40 STRESS-RELAXATION CURVES (150-180°C)

The *relaxation times* (τ*) derived from these tests are synthesized in Table 6. A significant deviation from the general trend was observed for the 60/40 (glycerol/AESO) system (Figure 45). Unlike the lower-oil-content analogs, this specific formulation failed to undergo measurable stress relaxation during the test duration. Consequently, it was not possible to calculate the relaxation times for this specific composition.

This lack of responsiveness in the 40% AESO sample can be attributed to its high cross-linking density. As previously shown by the FTIR analysis (DC% of 88.65%), this network is very dense, which likely restricts the movement of the polymer chains and slows down the bond-exchange reactions. To overcome this, future tests could be performed using longer observation times or by further increasing the catalyst amount to help the network rearrange more easily.

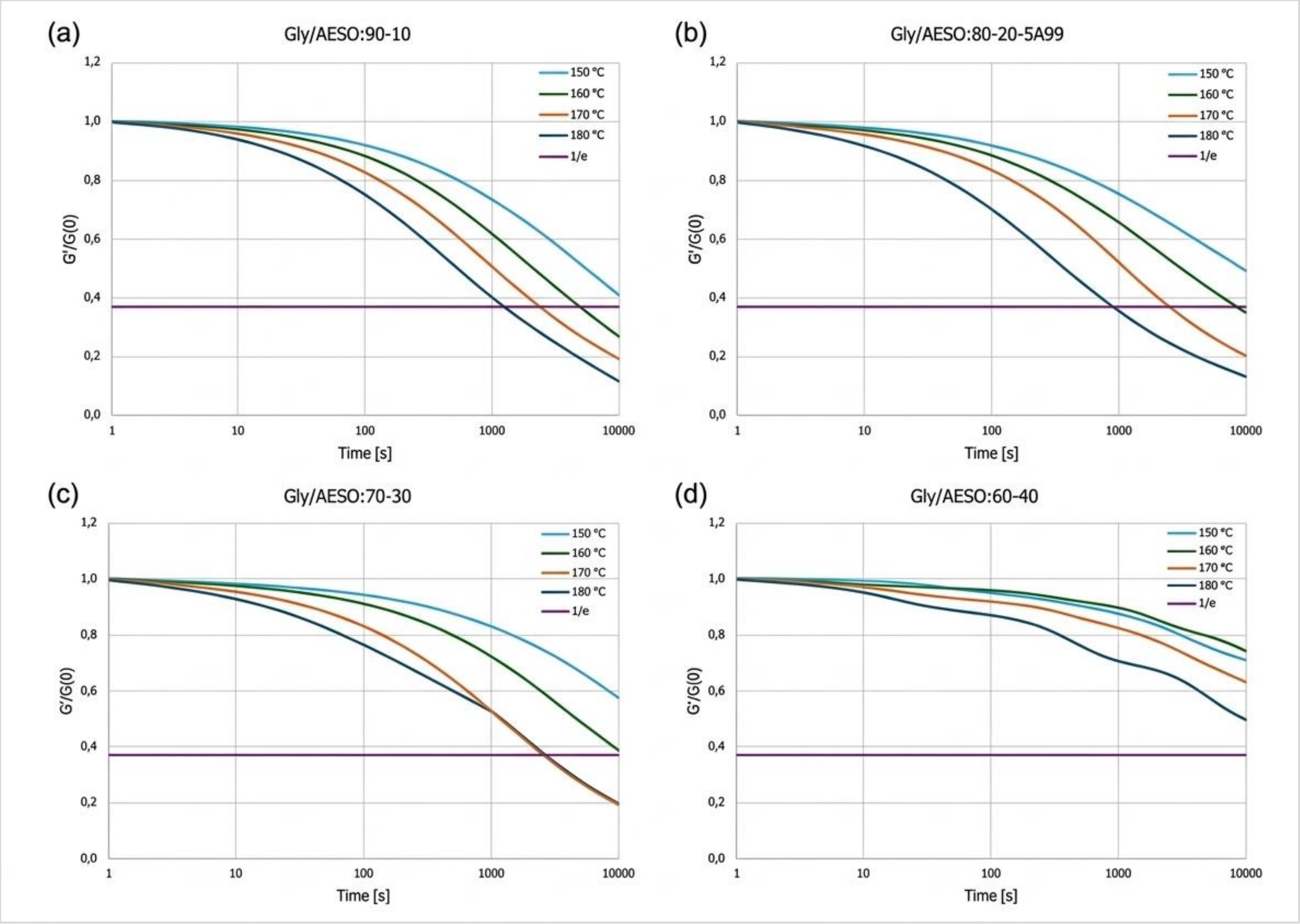

Figure 46 - *Normalized stress-relaxation behavior of the 3D-printed bio-b. vitrimers comparison* Evolution of the normalized storage modulus (G'/G0) as a function of time (s) for Glycerol/AESO networks with varying monomer ratios: (a) 90-10, (b) 80-20, (c) 70-30 and (d) 60-40.
The relaxation tests were performed at isothermal temperatures of 150°C, 160°C, 170°C and 180°C, to evaluate the temperature-dependent topological rearrangement driven by transesterification. For each composition, a consistent acceleration in relaxation kinetics is observed with increasing temperature, typical of an Arrhenius-like thermally activated process.
The horizontal purple line indicates the characteristic relaxation threshold where the modulus is reduced to 1/e (approximately 0.37) of its initial value, used to determine the characteristic relaxation time (τ*). A progressive shift towards longer relaxation times is evident as the AESO content increases, reflecting a higher cross-linking density and reduced segmental mobility within the more rigid 60-40 network.

Table 6 - Relaxation times (τ*) in the temperature range 150-180°C for the different Gly/AESO specimens

	Relaxation times [s]			
Sample	**τ*(150°C)**	**τ*(160°C)**	**τ*(170°C)**	**τ*(180°C)**
Gly/**AESO**:90-**10**	/	5090	2300	1270
Gly/**AESO**:80-**20**	/	8320	2540	890
Gly/**AESO**:70-**30**	/	10000	2620	/
Gly/**AESO**:60-**40**	/	/	/	/

To further investigate the temperature dependence of the bond-exchange kinetics, the *relaxation times* (τ*), obtained from the stress-relaxation tests (Table 6), were analyzed using the *Arrhenius model*, by plotting the natural logarithm of the relaxation times against the inverse of the temperature, multiplied by 1000 for scaling purposes (Figure 47). A linear relationship between ln(τ*) and 1/T was observed for all responding formulations, showing high correlation coefficients (R^2). This *Arrhenius-like* trend confirms that the network rearrangement is a thermally activated process, which is a fundamental characteristic of vitrimeric materials. Unlike traditional thermoplastic polymers, that may follow a non-linear *Williams-Landel-Ferry* (WLF) behavior, these systems maintain a constant *activation energy* (Ea) throughout the studied temperature range. This suggests that the macroscopic flow of the material is directly controlled by the rate of the exchange reactions (transesterification), rather than by simple chain segment mobility.

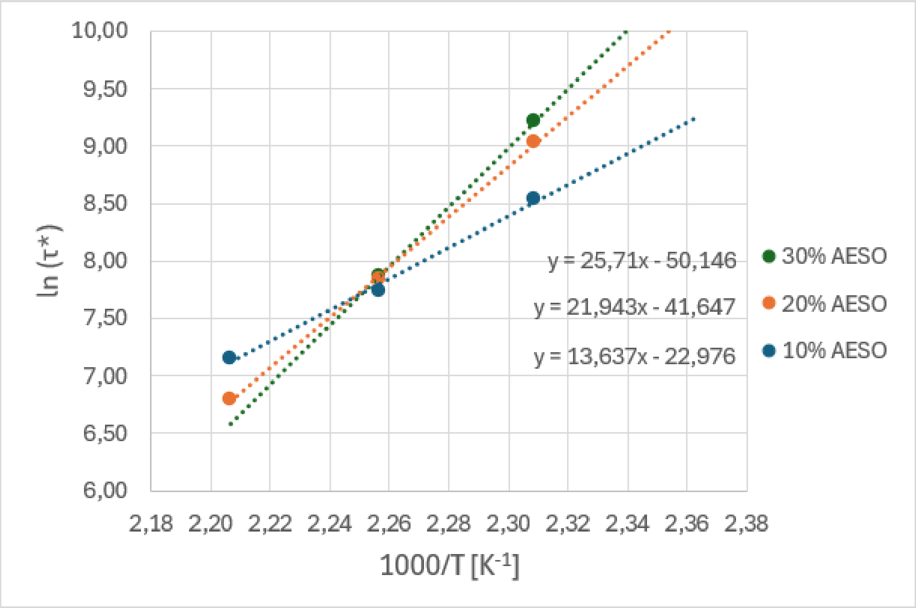

Figure 47 - Arrhenius plots for the different Gly/AESO samples (90/10, 80/20, 70/30) - The solid lines represent the linear fits used to calculate the activation energies (Ea)

The *activation energy* (Ea), for each vitrimeric system, was calculated from the *slope* (m) of the linear fits ($E_a = m * R$; where R is the *universal gas constant*). These values provided insight into the energy barrier that must be overcome to trigger the transesterification-driven flow.

TABLE 7 - ACTIVATION ENERGY (EA) CALCULATED FROM THE ARRHENIUS PLOTS FOR THE DIFFERENT GLY/AESO SPECIMENS

Sample	Slope (m)	Calculation (m · R)	Ea [kJ/mol]
Gly/**AESO**:90-**10**	13.64	13.64 · 8.314	113.38
Gly/**AESO**:80-**20**	21.94	21.94 · 8.314	182.43
Gly/**AESO**:70-**30**	25.71	25.71 · 8.314	213.75
Gly/**AESO**:60-**40**	X	x	x

As shown in Table 7, the *activation energy* (Ea) values vary with the AESO content, reflecting how the chemical composition and the cross-linking density influence the mobility of the dynamic network. Data reveal a significant increase in Ea as the soybean oil content rises from 10% to 30% (with values increasing from 113.38 kJ/mol to 213.75 kJ/mol). This trend suggests that higher AESO concentrations lead to a more densely cross-linked and stable network, which effectively raises the energy barrier required to trigger the dynamic exchange of covalent bonds. In the 10% AESO system, the relatively lower Ea suggests a more mobile environment, where transesterification exchanges can occur with less hindrance. Conversely, as the concentration of AESO rises, the network becomes significantly more rigid and densely packed. Consequently, higher thermal energy is required to trigger the bond-exchange reactions and enable macroscopic flow.

Furthermore, the slope of the linear fits becomes visibly steeper as the soybean oil percentage increases, indicating that the relaxation rate of the 30% AESO formulation is much more sensitive to temperature changes compared to the 10% AESO system.

In conclusion, these results demonstrate that while the chemical mechanism of transesterification remains constant (as evidenced by the linear Arrhenius-like behavior observed across all samples), the topology of the network plays a crucial role in defining the relaxation kinetics. This linear trend confirms that the exchange reactions are the kinetic bottleneck for network rearrangement, regardless of the AESO content. However, the significant increase in Ea highlights how a denser and more constrained network architecture imposes a higher energy barrier for these bond-shuffling processes to occur.

3.5 *Glass transition temperature* (Tg) determination

3.5.1 Differential scanning calorimetry (DSC) analysis

The thermal behavior of the glycerol/AESO vitrimer formulations was investigated via DSC, and the resulting thermograms are presented in Figure 48. A primary observation is the high degree of overlap between the first and second heating scans for all samples. This consistency indicates that the materials reached full conversion during the initial curing process, showing no evidence of post-curing phenomena or significant enthalpic relaxations. Such thermal stability confirms the robustness of the synthesized networks.

For these highly cross-linked vitrimeric systems, particularly those with higher AESO content (70-30 and 60-40), the change in *specific heat* at the *glass transition* (Tg) manifests as a slight variation in the slope of the curves, spread over a broad temperature interval. Despite this, it was possible to identify specific Tg intervals, all located below 0 °C, within a window spanning from -55°C to -25 C.

As the AESO concentration increases, a progressive shift of the Tg intervals toward higher temperatures is observed. This trend confirms that the incorporation of AESO effectively restricts chain mobility by increasing the cross-linking density and structural rigidity of the network. These findings are in excellent agreement with the higher *activation energy* (Ea) values discussed in the previous section.

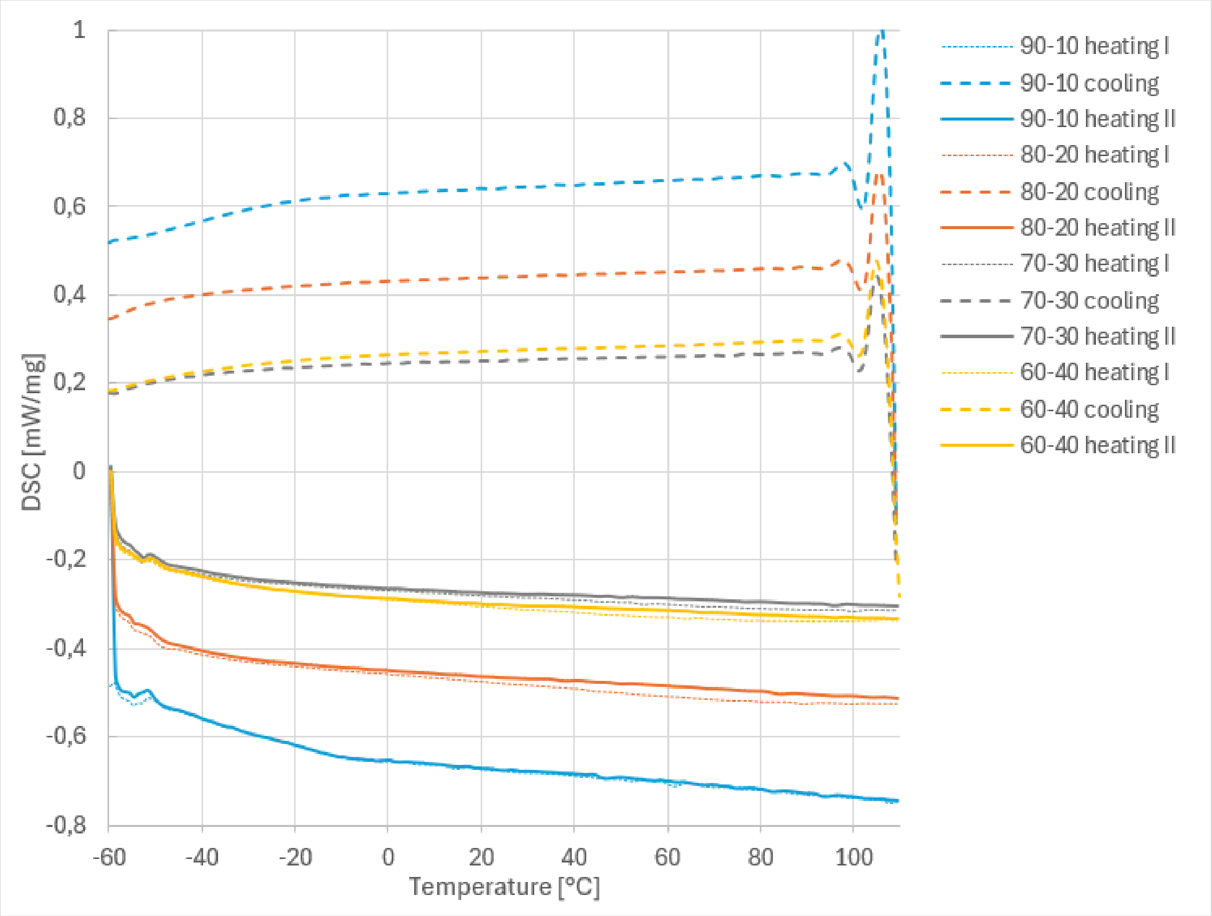

FIGURE 48 - DSC THERMOGRAMS COMPARISON

3.5.2 Dynamic-mechanical thermal analysis (DMTA)

The dynamic-mechanical properties of the glycerol/AESO vitrimers were further investigated through the temperature dependence of the *storage modulus* (E’) and the *loss factor* (tanδ).

At low temperatures (below -60°C), all samples exhibit a rigid glassy state, with a *storage modulus* (E’) exceeding 10^3 MPa. Upon heating, the sharp decrease in E’ and the corresponding peaks in the tanδ curves mark the glass transition. E’ and tanδ curves are shown in Figure 49, while Table 8 reports the *glass transition temperatures* (Tg), evaluated at the peaks of the tanδ curves.

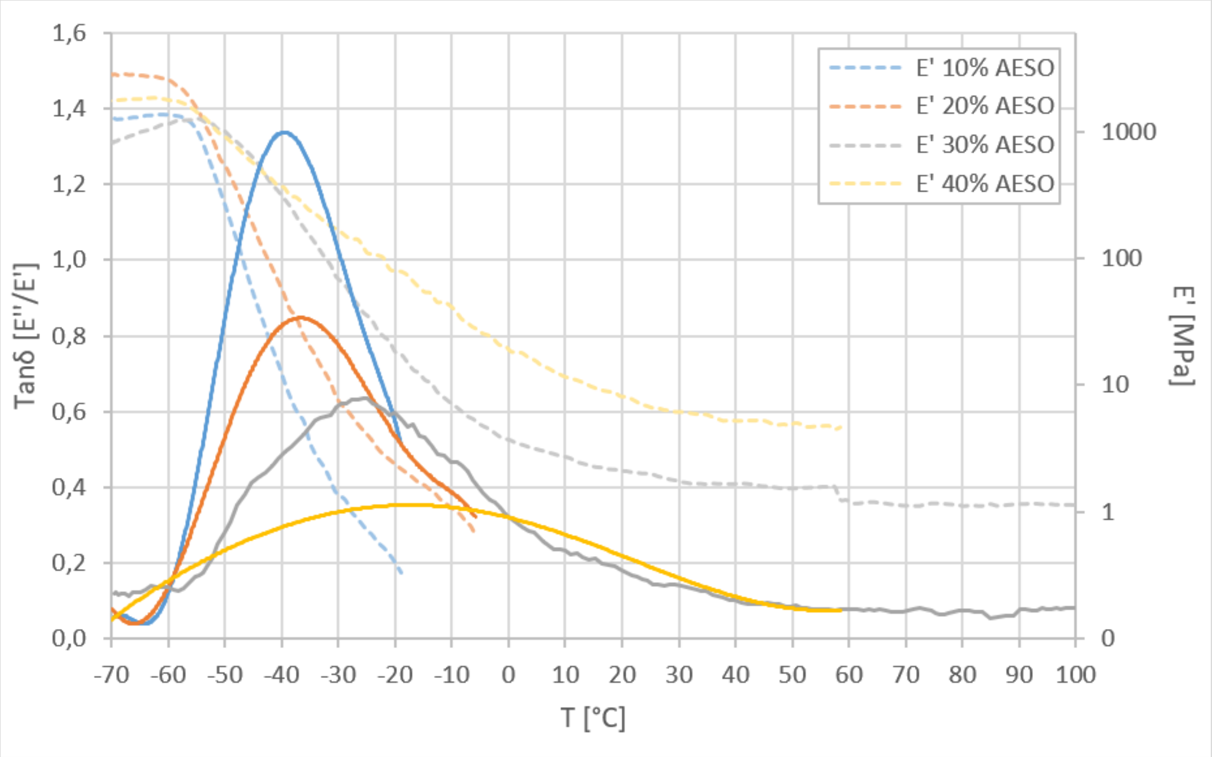

Figure 49 - Storage modulus (E’) and tan-δ (E”/E’) curves comparison

	10% AESO	20% AESO	30% AESO	40% AESO
Tg [°C]	-39	-36	-27	-15

Table 8 - Glass transition temperature (Tg) for the different Gly/AESO specimens

A clear trend (consistent with the DSC and Arrhenius analysis results) is observed as the AESO content increases: tanδ peaks shift toward higher temperatures and become significantly broader and lower in intensity. The reduction in peak height (from approximately 1.3 for the 10% AESO sample to 0.35 for the 40% formulation) indicates a transition from a more dissipative network to a highly constrained, elastic one. The broadening of the peaks (notably for the 30% and 40% AESO-based samples) suggests a more heterogeneous network structure due to the complex molecular architecture of AESO. [51, 52]

While the glass transition is clearly visible for all formulations, it should be noted that the curves for the 10% and 20% AESO samples do not reach the rubbery plateau due to the failure of the specimens during the test. In contrast, the 30% and 40% AESO samples show a stable rubbery region, allowing for the evaluation of their storage modulus at higher temperatures. In particular, the 40% AESO sample exhibits a significantly higher plateau modulus compared to the 30% formulation, confirming an increase in the network structure density as the AESO percentage rises. These increased structural rigidity and tighter network architecture explain the higher energy barriers (Ea) observed in the stress-relaxation experiments: in a more tightly bound network, the topological rearrangement via transesterification becomes more hindered, requiring more thermal energy to allow the bond-exchange process to proceed.

3.6 Self-healing experiment results

The results of the scratch-repair test for the Gly/AESO:80-20 formulation are illustrated in the figures below (Figure 50 - 51 - 52).

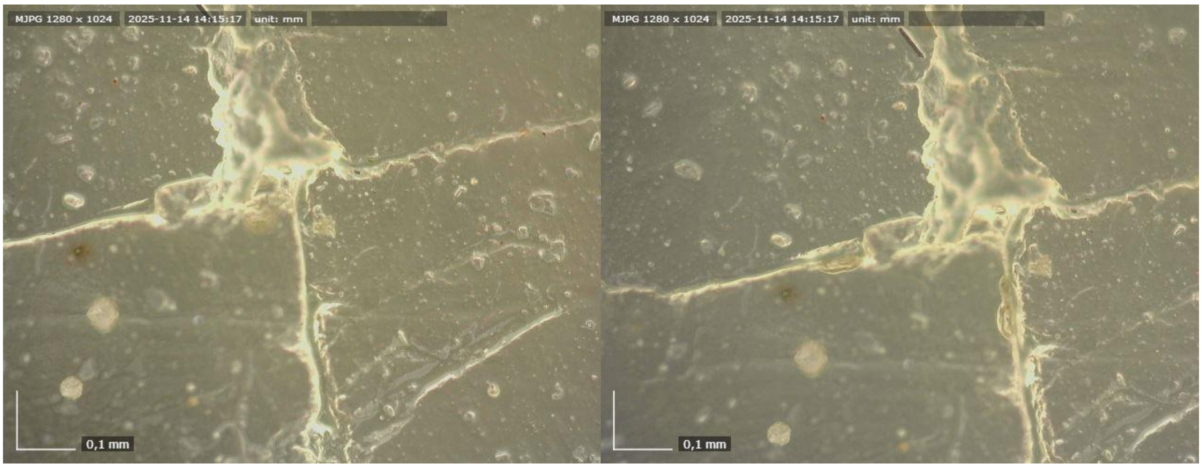

Figure 50 - *Initial state and early healing stage (0 min – 4 min)*: Optical micrographs of the 20% AESO sample showing the manually inflicted scratch at the beginning of the test (left) and after 4 minutes of thermal activation at 180°C (right)

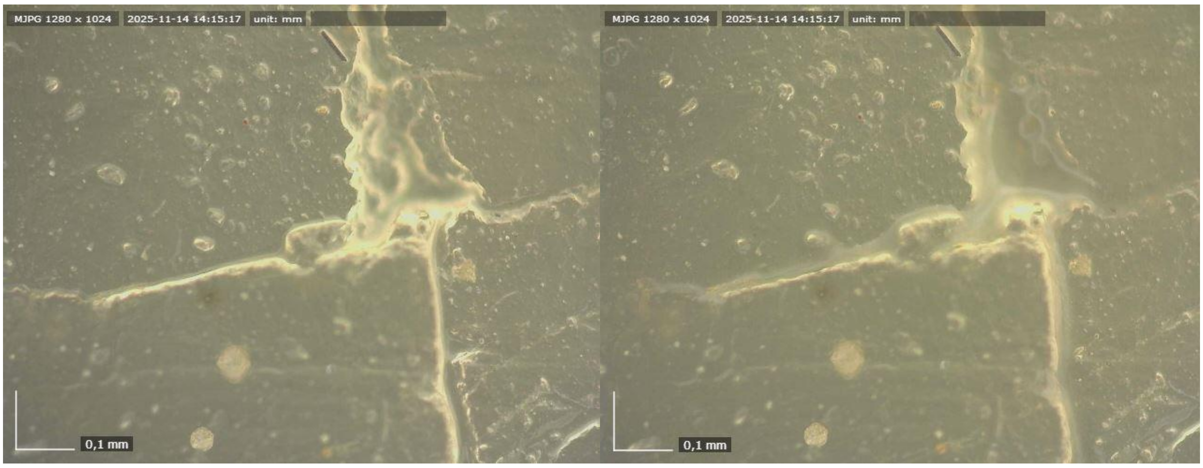

Figure 51 - *Intermediate healing stage (6 min – 8 min)*: Progressive closure of the scratch after 6 minutes (left) and 8 minutes (right)

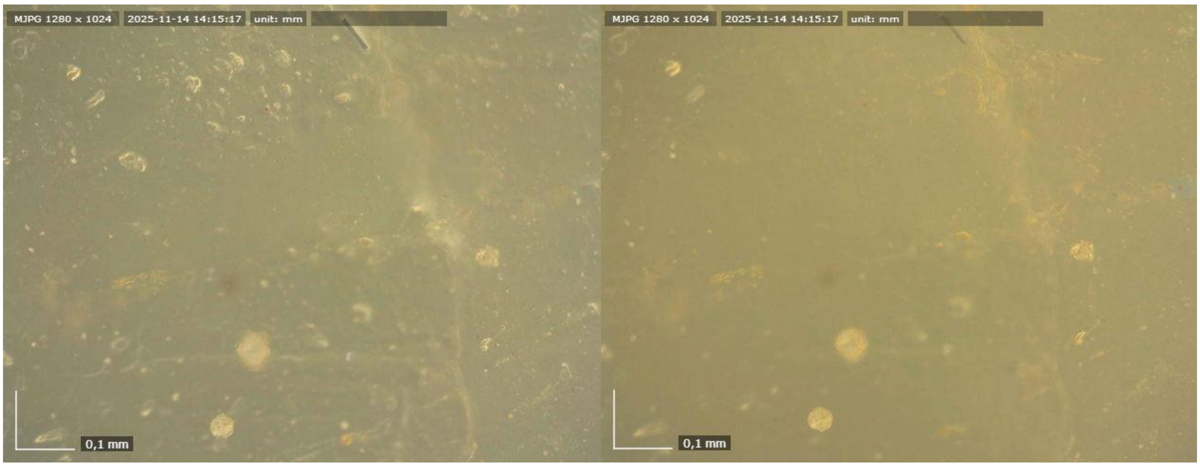

Figure 52 - *Advanced healing and final recovery (10 min – 15 min)*: View of the interface after 10 minutes (left) and after 15 minutes, at the conclusion of the thermal treatment (right)

The optical micrographs captured by the digital microscope provide clear evidence of the vitrimer's ability to recover from surface damage.

Immediately after the manual incision, the scratch appears as a well-defined, bright furrow with sharp edges, representing a significant interruption in the surface continuity. Upon thermal activation at 180°C for 15 minutes, a progressive "filling" of the damaged area is observed. The sharp boundaries of the scratch gradually blur and eventually disappear as the material flows into the void. This macroscopic recovery is driven by the internal rearrangement of the network via associative transesterification reactions. At 180°C, the exchange rate is sufficiently high to allow for a localized flow of the polymer chains across the scratch interface. Furthermore, the high surface quality of the repaired area suggests that the material maintains its structural integrity while undergoing topological changes.

The successful healing observed within 15 minutes aligns perfectly with the previously discussed stress-relaxation data, which identified a characteristic *relaxation time* (τ^*) of 14.8 minutes at 180°C for the Gly/AESO:80-20 formulation, confirming that the time required for macroscopic repair is closely related to the characteristic relaxation time of the vitrimeric network.

3.7 Mechanical performance analysis

3.7.1 Impact strength: Izod test results

The results of the Izod impact tests highlighted a clear dependence of the impact resistance on the composition of the glycerol/AESO-based vitrimers. The normalized *Izod impact strength* (a_k) values, summarized in the bar chart below (Figure 53), showed a progressive increase as the AESO fraction rises, indicating an enhancement in the material's ability to dissipate energy during impact fracture.

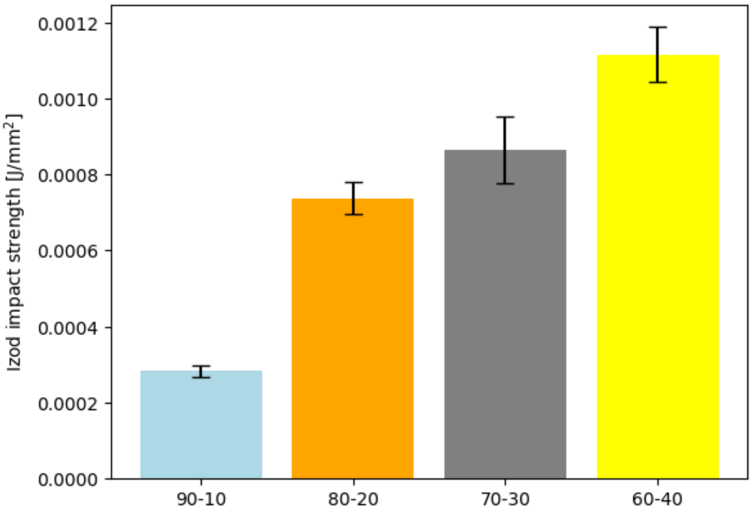

FIGURE 53 - AVERAGE ENERGY ABSORBED DURING IZOD IMPACT TESTS, NORMALIZED BY THE RESIDUAL CROSS-SECTIONAL AREA AT THE NOTCH, FOR THE DIFFERENT GLY/AESO SAMPLES (ERROR BARS REPRESENT THE STANDARD DEVIATION ACROSS FIVE SPECIMENS PER FORMULATION)

In particular, the samples with composition 90-10 (glycerol/AESO) exhibit the lowest average impact strength (0.000283 ± 0.000015 J/mm²), indicating a highly brittle behavior. The low standard deviation suggests good experimental reproducibility, while simultaneously confirming the limited intrinsic capacity of this formulation to absorb energy prior to fracture. Increasing the AESO content leads to a significant enhancement in impact strength: the 80-20 samples exhibit an average value of 0.000738 ± 0.000043 J/mm², approximately 2.6 times higher than that of the 90-10 formulation. For the 70-30 formulation, the average absorbed energy further increases to 0.000866 ± 0.000087 J/mm². In this case, a slightly higher data dispersion is also observed, which may indicate a greater sensitivity of the material's microstructure to minor variations in specimen preparation or phase distribution. The maximum impact strength is observed for the 60-40 formulation, which exhibits an average value of 0.001116 ± 0.000069 J/mm².

These results suggest that the introduction of larger AESO fractions contributes to the development of a network structure more effective at dissipating impact energy, likely due to the increased cross-linking density. Consequently, modulating the glycerol/AESO ratio represents a critical parameter for optimizing the material's impact mechanical properties: while soybean oil plays a key role in enhancing toughness, higher glycerol concentrations appear, conversely, to promote brittle fracture mechanisms, thereby reducing the system's ability to absorb energy prior to failure.

3.7.2 Tensile properties: stress-strain analysis

The mechanical performance of the Gly/AESO vitrimers was further evaluated through uniaxial tensile tests. The results, summarized in Table 9, revealed a significant and progressive enhancement in stiffness, strength, and ductility as the concentration of epoxidized soybean oil (AESO) increases within the polymer network.

TABLE 9 - MECHANICAL PROPERTIES OF GLYCEROL/AESO VITRIMERS OBTAINED FROM UNIAXIAL TENSILE TESTS, INCLUDING YOUNG'S MODULUS, TENSILE STRENGTH AND ELONGATION AT BREAK. DATA ARE PRESENTED AS MEAN VALUES ± STANDARD DEVIATION. NOTE: FOR THE 90-10 SAMPLE, THE STANDARD DEVIATION IS NOT REPORTED AS ONLY ONE OF THE FIVE TESTED SPECIMENS YIELDED A VALID RESULT.

Sample	**Young's modulus (E) [MPa]**	**Tensile strength (σ_{max}) [MPa]**	**Elongation at break (ε_b) (%)**
Gly/**AESO**:90-**10**	0.3	0.015	0.61
Gly/**AESO**:80-**20**	0.72 ± 0.12	0.13 ± 0.03	10.12 ± 1.87
Gly/**AESO**:70-**30**	1.85 ± 0.18	0.29 ± 0.04	13.55 ± 1.70
Gly/**AESO**:60-**40**	4.80 ± 0.21	0.82 ± 0.14	16.32 ± 2.42

The *Young's modulus* (E) exhibits a remarkable increase, rising from 0.3 MPa for the 90-10 formulation to 4.80 ± 0.21 MPa for the 60-40 sample (Figure 54A). This sixteen-fold increase in stiffness suggests that AESO acts as a highly effective cross-linking agent, promoting the formation of a denser and more rigid three-dimensional network.

A similar trend is observed for the *tensile strength* ($\sigma_{\max}$): the 90-10 formulation shows a very low resistance to traction (0.015 MPa), indicative of a fragile and poorly cohesive network. However, by increasing the AESO content to 40%, the tensile strength reaches 0.82 ± 0.14 MPa (Figure 54B). This improvement confirms that the incorporation of longer fatty acid chains from the soybean oil reinforces the matrix, allowing the material to withstand significantly higher loads before structural failure.

One of the most striking results is the impact of AESO on the *elongation at break* (ε_b): the 90-10 sample behaves as a typical brittle material, with a negligible elongation of only 0.61%; in contrast, the 60-40 formulation achieves an elongation of 16.32 ± 2.42% (Figure 54C).

This transition from a brittle to a more ductile-like behavior indicates that the AESO-rich networks are capable of significant plastic deformation, which effectively dissipates energy. The long, flexible chains of soybean oil likely provide the necessary segmental mobility to prevent premature crack propagation, a finding that aligns perfectly with the results obtained in the Izod impact tests.

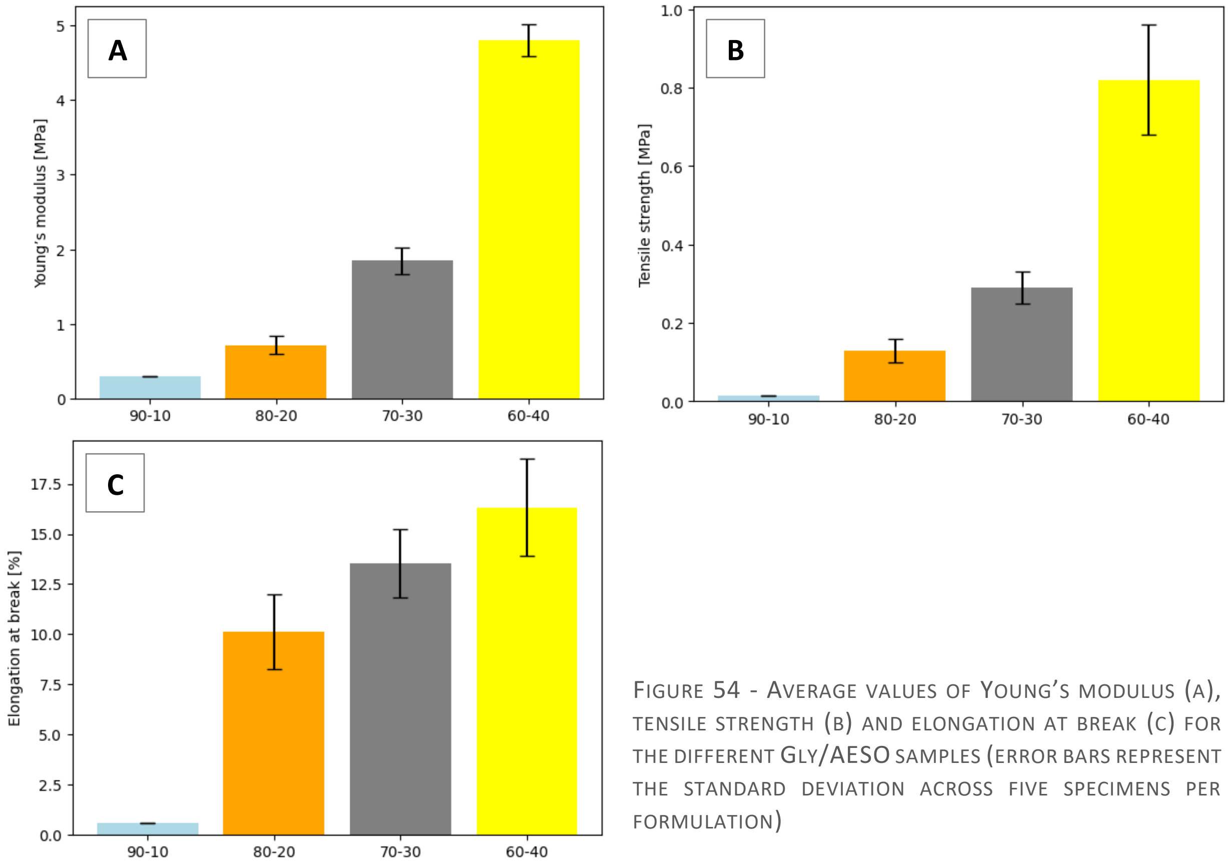

FIGURE 54 - AVERAGE VALUES OF YOUNG'S MODULUS (A), TENSILE STRENGTH (B) AND ELONGATION AT BREAK (C) FOR THE DIFFERENT GLY/AESO SAMPLES (ERROR BARS REPRESENT THE STANDARD DEVIATION ACROSS FIVE SPECIMENS PER FORMULATION)

The standard deviation values reported in Table 9 provide further insight into the structural homogeneity and reproducibility of the synthesized materials. Samples containing 20% and 30% AESO exhibit moderate data dispersion, likely reflecting a transition phase in the network architecture: in this regime, small local fluctuations in the distribution of AESO long chains can significantly influence the specific point of fracture. In contrast, the 40% AESO formulation maintains a relatively low standard deviation for its Young's Modulus, suggesting that a higher concentration of the epoxidized oil promotes a more uniform and stable network throughout the bulk of the material. Finally, the absence of a standard deviation for the 10% AESO sample is a direct consequence of its extreme fragility. Its high brittleness led to premature failure during specimen gripping or at the very onset of the tensile test, resulting in only one valid measurement out of the five specimens tested. This underscores that a minimum threshold of AESO is required to ensure sufficient mechanical integrity for reliable characterization.

In conclusion, the modulation of the Gly/AESO ratio allows for precise control over the mechanical profile of the vitrimer: while the glycerol-rich formulations result in weak and brittle networks, the addition of AESO systematically shifts the material towards a "tougher" regime, characterized by a simultaneous increase in Young’s modulus, strength, and elongation at break. This synergistic improvement is a clear indicator of a more robust and well-integrated network architecture.

3.7.3 Summary of mechanical behavior

Mechanical characterization via tensile and Izod impact tests highlights a consistent trend, while simultaneously exposing the inherent mechanical limitations of these specific glycerol/AESO-based formulations.

While the increasing fraction of AESO clearly improves the network's integrity, shifting it from an extremely brittle state to a more cohesive and ductile regime, the absolute values for stiffness and strength remain notably low. With a maximum Young’s modulus of only 4.80 MPa and a tensile strength failing to reach 1 MPa, these vitrimers exhibit poor structural performance compared to conventional thermosets or engineering plastics.

However, these "sub-optimal" mechanical properties must be interpreted within the context of the material's high glycerol content and its primary focus on sustainability and dynamic functionality. These systems should be viewed not as high-strength structural materials, but rather as proof-of-concept bio-based networks, where mechanical robustness has been secondary to achieving a fully renewable and reprocessable architecture. Future optimizations, perhaps through higher cross-linking densities or the incorporation of reinforcing fillers, would be strictly necessary to bridge the gap toward practical applications.

3.8 Reprocessing tests results

The reprocessing capability of the synthesized vitrimer networks was preliminarily evaluated through thermal welding experiments performed on fractured “dog-bone” tensile specimens. The intermediate formulations Gly/AESO 80-20 and 70-30 were selected for this investigation, as they exhibited the best compromise between dynamic bond exchange, in the stress-relaxation tests, and baseline mechanical properties (such as stiffness, strength, and ductility) in the tensile and Izod tests.

After the reprocessing cycle (180°C, 30 min, 200 bar), visual inspection of the specimens revealed that the two fractured halves were successfully welded together in the central region corresponding to the original fracture interface. This observation suggests that the applied thermal and mechanical conditions were sufficient to activate the transesterification-driven bond exchange reactions characteristic of vitrimer networks, allowing interfacial molecular rearrangement and partial structural recovery.

However, despite the apparent re-bonding at the fracture interface, the specimens exhibited multiple new fractures located near the extremities of the dog-bone geometry, which were not present prior to the reprocessing step. During the removal of the samples from the mold, these newly formed cracks propagated, causing the detachment of both extremities from the central welded region. As a result, the specimens could not be subjected to a second tensile test, preventing a quantitative evaluation of the mechanical recovery. A schematic representation of the reprocessing experiments is illustrated in Figure 55.

The formation of secondary fractures is likely related to stress concentration and mechanical constraints imposed by the mold during the hot-pressing step. In particular, the narrow cross-section of the dog-bone geometry may have experienced non-uniform stress distribution under the applied pressure, leading to localized damage in the thinner regions near the specimen shoulders. Additionally, thermal gradients and differential shrinkage during cooling may have contributed to the generation of internal stresses, further promoting crack initiation in these areas.

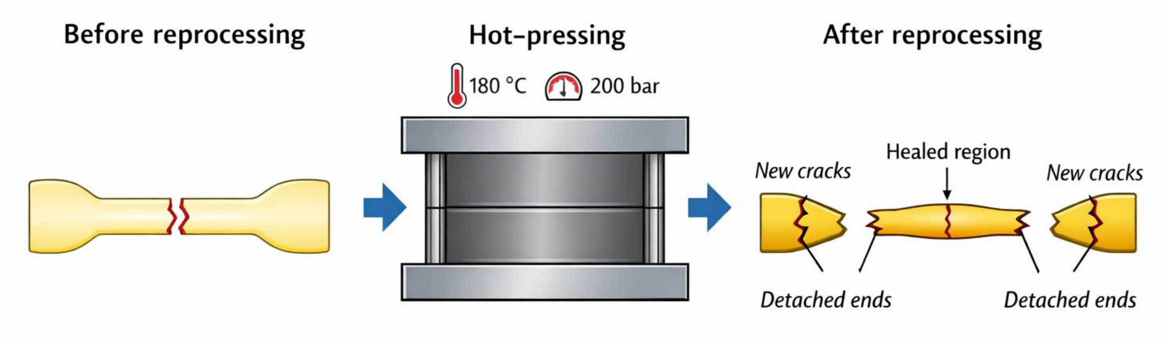

FIGURE 55 - SCHEMATIC REPRESENTATION OF THE REPROCESSING EXPERIMENT PERFORMED ON FRACTURED GLYCEROL/AESO VITRIMER SPECIMENS. THE ORIGINAL DOG-BONE SAMPLE, FRACTURED DURING TENSILE TESTING, WAS SUBJECTED TO A HOT-PRESSING CYCLE (180°C, 30 MIN, 200 BAR) TO PROMOTE TRANSESTERIFICATION-DRIVEN BOND EXCHANGE REACTIONS. ALTHOUGH WELDING OCCURRED AT THE ORIGINAL FRACTURE INTERFACE, SECONDARY CRACKS DEVELOPED NEAR THE SPECIMEN EXTREMITIES, LEADING TO THE DETACHMENT OF THE ENDS DURING REMOVAL FROM THE MOLD.

Although the experiment did not allow a quantitative assessment of property recovery, the successful welding observed at the original fracture interface provides qualitative evidence that dynamic bond exchange reactions were effectively activated under the selected reprocessing conditions. Future experiments could therefore focus on optimizing the reprocessing protocol, for instance by reducing the applied pressure, modifying the mold geometry, or reprocessing specimens with simpler shapes, in order to minimize stress concentrations and prevent secondary fracture. Additionally, increasing the AESO content and the catalyst concentration could enhance the material's ductility and lower the required reprocessing temperature. Such refinements would be essential to transform these bio-based networks into truly reprocessable materials, capable of maintaining their structural integrity across multiple recycling cycles.

4. Conclusion and future perspectives

The present work investigated the development of a photocurable vitrimeric resin system suitable for LCD-based additive manufacturing, relying on renewable monomers derived from glycerol and soybean oil: *glycerol 1,3-diglycerolate diacrylate* (GDGDA) and *acrylated epoxidized soybean oil* (AESO). The study was motivated by the increasing need to reconcile the technological advantages of photopolymer-based 3D printing with the broader objectives of sustainability, material circularity, and functional durability. Within this framework, the results obtained throughout this research demonstrate that bio-based vitrimer networks can be successfully integrated into vat photopolymerization processes, while maintaining both structural integrity during printing and the dynamic characteristics required for network rearrangement. The overall findings, therefore, provide clear evidence for the feasibility of combining bio-derived feedstocks, dynamic covalent chemistry, and high-resolution additive manufacturing within a single materials platform.

The first major outcome of this work concerns the successful formulation and processing of the GDGDA/AESO resin systems. All investigated compositions exhibited effective photocuring behavior and were compatible with LCD printing conditions, after the optimization of exposure parameters through Jacob’s working curves. Most importantly, the intermediate formulations, particularly 80/20 and 70/30, were able to reproduce thin-walled hollow spheres with patterned lattice-like geometries, confirming that these resins possess adequate reactivity and rheological characteristics to support reliable layer-by-layer construction. The printed parts showed high geometric definition, no collapse of delicate struts, and no internal clogging after washing, indicating that the curing kinetics and light penetration, characteristics of the formulations, were well suited for the adopted printing strategy. These results are particularly meaningful considering the high bio-based content of the system, as bio-derived monomers are often associated with challenges related to viscosity, reactivity, or network uniformity. In this case, however, the formulations proved sufficiently robust to enable stable processing without the need for complex additives or extensive modification of the printing procedure.

The spectroscopic and photorheological analyses further confirmed the effectiveness of the curing process and provided valuable insight into the network formation mechanism. All compositions achieved high double-bond conversion values, exceeding 87%, which indicates that the photopolymerization reaction proceeded efficiently across the explored compositional range. At the same time, the gradual increase in AESO content resulted in faster gelation and higher final storage modulus values during irradiation, demonstrating the ability of the soybean-oil-derived component to promote a denser and mechanically stronger network. These observations highlight the synergistic role of the two monomers, where the glycerol-derived component contributes to network flexibility and functional group availability, while AESO enhances crosslinking efficiency and structural reinforcement. The resulting materials, therefore, represent a well-balanced compromise between processability, reactivity, and network formation.

The dynamic behavior of the networks represents one of the strongest scientific contributions of the thesis. Stress-relaxation experiments performed between 150 and 180°C confirmed that transesterification can effectively drive topological rearrangement in these bio-based systems, but also that this capability is extremely sensitive to both catalyst content and network composition. The catalyst study on the 80/20 system showed that 5 phr of Miramar A99 was essential to obtain meaningful stress dissipation, whereas the uncatalyzed and 2.5 phr variants showed negligible or incomplete relaxation. This establishes a practical threshold for activating vitrimer-like flow under the explored conditions and confirms the indispensable role of the catalyst in reducing the kinetic barrier of bond exchange. Among the standard formulations, the relaxation times reflected a non-trivial balance between mobility and network density: while the 30% AESO formulation relaxed more slowly, than the 10% and 20% AESO ones, the 60/40 system did not reach measurable relaxation within the entire test window. Taken together with the Arrhenius plots for the responding systems, these results underscored a crucial point: the exchange chemistry remained vitrimer-like and thermally activated across the investigated range, but the energy barrier to macroscopic rearrangement increased sharply with AESO content, as the denser structure prevented easy movement of the polymer chains. Therefore, increasing AESO improves rigidity and strength, yet simultaneously penalizes reconfigurability. Identifying this trade-off was a central outcome of this thesis, as it defined the primary relationship between the material’s structure and its final properties.

The macroscopic self-healing experiment provided even more direct evidence of the dynamic behavior of the networks. For the 80/20 formulation, a surface scratch progressively disappeared during thermal treatment at 180°C, and complete repair was observed after 15 minutes. The study correctly linked this healing time to the stress-relaxation result of approximately 14.8 minutes at the same temperature, thereby showing a direct correspondence between molecular relaxation kinetics and macroscopic damage recovery. This agreement is highly meaningful because it demonstrates that the characteristic relaxation time is not only a rheological parameter but also a physically useful predictor of self-healing behavior. In broader terms, it confirms that these networks are capable of localized flow and interface reconstruction without loss of integrity, which is precisely the kind of functionality that makes vitrimers attractive for sustainable manufacturing. The ability of a 3D-printed bio-based thermoset to autonomously reduce surface damage, through thermal activation, illustrates the practical potential of vitrimer chemistry for extending the service life of printed components and reducing material waste associated with premature failure.

The thermal and viscoelastic characterization clarified the nature of these materials in service conditions. The glass transition temperatures remained below room temperature for all formulations, ranging from approximately -39°C to -15°C, which indicates that the printed networks behave in a rubbery state under ambient conditions. This aspect helps explain the relatively low stiffness and strength measured in tension, even for the most cross-linked composition. The mechanical data showed a clear and systematic improvement with increasing AESO content, moving from the extremely fragile 90/10 formulation to the significantly more cohesive 60/40 system. Even so, the absolute values remained modest, with a maximum Young’s modulus of 4.80 MPa and a tensile strength below 1 MPa. While the dynamic behavior and the renewable character of the system are valuable, the current mechanical profile restricts the immediate application potential to soft components, low-load devices, or demonstrative prototypes. The study, therefore, succeeds in establishing a sustainable and reprocessable photopolymer concept, but it also makes clear that further formulation development is necessary before the material can compete with more established additive-manufacturing resins.

The reprocessing experiments provided preliminary indications of the recyclability potential of the material. The hot-pressing test showed that fractured specimens could be rejoined through thermal treatment, suggesting that bond exchange reactions enable interfacial welding between damaged surfaces. Even though secondary cracking, near the specimen edges, prevented a full mechanical reassessment of the reprocessed samples and a reliable quantitative comparison with the original material as well, the visible fusion of the fragments nevertheless indicates that dynamic rearrangement remains active during reprocessing. Further optimization of the molding geometry and experimental procedure would likely allow a more accurate evaluation of the mechanical recovery after recycling.

Taken together, the results of this thesis show that the most successful formulations are not necessarily the ones with the highest mechanical properties or the fastest bond exchange, but those located in the intermediate compositional window where printability, dynamic response and baseline integrity coexist. In this sense, the 80/20 and 70/30 systems appear as the most balanced candidates for further development. The 60/40 network offered the best mechanical behavior and the highest Tg, but it became too constrained to show measurable stress relaxation within the explored conditions. Conversely, the 90/10 network was more dynamically accessible but mechanically too fragile for reliable use. The scientific value of the work lies precisely in having mapped this trade-off with a systematic compositional study, thus establishing a rational path for future optimization.

Future research should therefore move in two complementary directions. The first is the kinetic optimization of exchange chemistry. Since the 60/40 formulation appears to be overconstrained under the present catalyst loading and thermal window, increasing the catalyst concentration, extending the relaxation time window, or exploring alternative transesterification catalysts could shift the system toward a more practical balance between rigidity and processability. A second route is network and formulation engineering, aimed at improving toughness and structural robustness without erasing vitrimeric mobility. This could include fine tuning of the glycerol/AESO ratio around the intermediate region, incorporation of flexible bio-based co-monomers, or the addition of reinforcing phases such as nano- or micro-fillers to increase strength and fracture resistance. Equally important will be the redesign of reprocessing protocols, for example by using simpler specimen geometries, lower pressure, better thermal homogeneity, or molds that minimize stress concentration at the shoulders, so that true recovery factors can be quantified in future tensile or fracture experiments. From an application standpoint, it will also be essential to investigate long-term thermal aging, repeated reprocessing cycles, dimensional stability, and the performance of printed lattices and architected structures, since these are the domains where additive manufacturing and vitrimer functionality can create the greatest added value.

In conclusion, this study establishes a solid experimental foundation for the development of sustainable vitrimeric resins compatible with LCD-based additive manufacturing. The successful demonstration of printability, high curing conversion, dynamic stress-relaxation, and self-healing capability confirms that the proposed Gly/AESO system represents a promising step toward more sustainable and functional photopolymer materials. Among these aspects, the self-repairing response represents one of the most promising features, as it directly addresses the intrinsic irreversibility that traditionally characterizes thermoset photopolymers. By enabling the relaxation and rearrangement of the network under thermal activation, the developed materials introduce the possibility of repairing damaged components, improving durability, and potentially extending the operational lifetime of printed structures. While further improvements are necessary to enhance mechanical robustness and fully exploit the recyclability potential, the results clearly show that bio-based vitrimer networks can offer a viable pathway toward additive manufacturing materials that combine performance, repairability, and reduced environmental impact.

Bibliography

[1] D. Montarnal, M. Capelot, F. Tournilhac, and L. Leibler, "Silica-Like Malleable Materials from Permanent Organic Networks," *Science*, vol. 334, no. 6058, pp. 965–968, Nov. 2011, doi: 10.1126/science.1212648.

[2] I. Dey and S. Bose, "Vitrimers: bridging the recycling gap between thermosets and thermoplastics," *J. Mater. Sci.: Compos.*, vol. 7, no. 1, 2026, doi: 10.1186/s42252-025-00086-6.

[3] W. Denissen, G. B. Winne, and F. E. Du Prez, "Vitrimers: permanent organic networks with glass-like fluidity," *Chem. Sci.*, vol. 7, no. 1, pp. 30–38, Jan. 2016, doi: 10.1039/c5sc02223a.

[4] C. Zhao et al., "Recyclable and self-healing vitrimers from biogenic raw materials," *Green Chem.*, vol. 20, no. 21, pp. 4955–4962, Oct. 2018, doi: 10.1039/C8GC02257G.

[5] M. Capelot, D. Montarnal, F. Tournilhac, and L. Leibler, "Metal-catalyzed transesterification for viable vitrimers," ACS Macro Lett., vol. 1, no. 7, pp. 789–792, 2012.

[6] F. I. Altuna, C. E. Hoppe, and R. J. J. Williams, "Epoxy vitrimers based on a dual-network strategy," RSC Adv., vol. 6, no. 91, pp. 88647–88655, 2016.

[7] C. J. Kloxin and C. N. Bowman, "Covalent Adaptable Networks: Smart, Reconfigurable and Responsive Network Systems," Chem. Soc. Rev., vol. 42, no. 17, pp. 7161–7173, 2013.

[8] Y. Yang, W. Zhang, and X. Zhang, "Thermally reversible polymer networks based on dynamic covalent bonds," *Adv. Mater.*, vol. 28, no. 31, pp. 6604–6617, 2016.

[9] P. Chakma and D. Konkolewicz, "Dynamic Covalent Bonds in Polymeric Materials," *Angew. Chem. Int. Ed.*, vol. 58, no. 29, pp. 9682–9695, 2019, doi: 10.1002/anie.201813525.

[10] J. M. Winne, L. Leibler, and F. E. Du Prez, "Dynamic covalent chemistry in polymer networks: a vitrimer standpoint," Polym. Chem., vol. 10, no. 45, pp. 6091–6108, 2019.

[11] M. Guerre, J. M. Winne, C. J. Kloxin, and F. E. Du Prez, "Vitrimers: current state-of-the-art and future challenges," Chem. Sci., vol. 11, no. 19, pp. 4855–4870, 2020.

[12] S. J. Garcia, "Effect of dynamic bond exchange rate of CANs on self-healing," Eur. Polym. J., vol. 106, pp. 118–133, 2018.

[13] B. R. Elling and W. R. Dichtel, "Reprocessable cross-linked polymer networks: are associative exchange mechanisms desirable?," *ACS Cent. Sci.*, vol. 6, no. 9, pp. 1488–1496, Sep. 2020, doi: 10.1021/acscentsci.0c00567.

[14] N. J. Van Zee and R. H. Grubbs, "Guanidine-Catalyzed Transesterification of Vitrimers," ACS Macro Lett., vol. 8, no. 1, pp. 57–62, 2019.

[15] J. Zheng, J. Yang, and J. S. Moore, "3D printing of vitrimers: Challenges and opportunities," Macromol. Rapid Commun., vol. 42, no. 13, p. 2100411, 2021.

[16] A. Mariani and G. Malucelli, "Biobased vitrimers: towards sustainability and circularity," *Chem. Commun.*, vol. 61, pp. 2173–2189, 2025, doi: 10.1039/D4CC05967K.

[17] X. Zhang and F. Liou, "Introduction to additive manufacturing," in Additive Manufacturing, Elsevier, 2021, pp. 1–31. doi: 10.1016/B978-0-12-818411-0.00009-4.

[18] L. J. Tan, W. Zhu, and K. Zhou, “Recent Progress on Polymer Materials for Additive Manufacturing,” Oct. 01, 2020, Wiley-VCH Verlag. doi: 10.1002/adfm.202003062.

[19] R. Chaudhary, P. Fabbri, E. Leoni, F. Mazzanti, R. Akbari, and C. Antonini, “Additive manufacturing by digital light processing: a review,” Apr. 01, 2023, Springer Science and Business Media Deutschland GmbH. doi: 10.1007/s40964-022-00336-0.

[20] J. Izdebska-Podsiadły, “Classification of 3D printing methods,” in Polymers for 3D Printing: Methods, Properties, and Characteristics, Elsevier, 2022, pp. 23–34. doi: 10.1016/B978-0-12-818311-3.00009-4.

[21] A. Davoudinejad, “Vat photopolymerization methods in additive manufacturing,” in Additive Manufacturing, Elsevier, 2021, pp. 159–181. doi: 10.1016/B978-0-12-818411-0.00007-0.

[22] M. Pagac et al., “A review of vat photopolymerization technology: Materials, applications, challenges, and future trends of 3d printing,” Feb. 02, 2021, MDPI AG. doi: 10.3390/polym13040598.

[23] M. Bergoglio, Z. Najmi, A. Cochis, M. Miola, E. Vernè, and M. Sangermano, “UV-Cured Bio-Based Acrylated Soybean Oil Scaffold Reinforced with Bioactive Glasses,” Polymers (Basel), vol. 15, no. 20, Oct. 2023, doi: 10.3390/polym15204089.

[24] N. Zhu et al., “Preparation of complex SiOC ceramics by a novel photocurable precursor with liquid crystal display (LCD) 3D printing technology,” J Eur Ceram Soc, vol. 42, no. 7, pp. 3204–3212, Jul. 2022, doi: 10.1016/j.jeurceramsoc.2022.02.026.

[25] H. W. Tan, A. R. Abdul Aziz, and M. K. Aroua, “Glycerol production and its applications as a raw material: A review,” *Renew. Sustain. Energy Rev.*, vol. 27, pp. 118–127, Nov. 2013, doi: 10.1016/j.rser.2013.06.035.

[26] T. Liu et al., “Glycerol Induced Catalyst-Free Curing of Epoxy and Vitrimer Preparation,” *Macromol. Rapid Commun.*, vol. 40, no. 7, p. 1800889, Apr. 2019, doi: 10.1002/marc.201800889.

[27] S. Grauzeliene, M. Kastanauskas, V. Talacka, and J. Ostrauskaite, “Photocurable Glycerol- and Vanillin-Based Resins for the Synthesis of Vitrimers,” *ACS Appl. Polym. Mater.*, vol. 4, no. 8, pp. 6103–6110, Aug. 2022, doi: 10.1021/acsapm.2c00884.

[28] S. Grauzeliene, A. S. Schuller, C. Delaite, and J. Ostrauskaite, “Development and Digital Light Processing 3D Printing of a Vitrimer Composed of Glycerol 1,3-Diglycerolate Diacrylate and Tetrahydrofurfuryl Methacrylate,” *ACS Appl. Polym. Mater.*, vol. 5, no. 9, pp. 6958–6965, Sep. 2023, doi: 10.1021/acsapm.3c00898.

[29] C. Noè et al., “DLP-printable fully biobased soybean oil composites,” *Polymer (Guildf)*, vol. 247, Apr. 2022, doi: 10.1016/j.polymer.2022.124779.

[30] Y. Li, X. Ren, L. Zhu, C. Li, and T. Lin, “Synthesis and characterization of polyurethane acrylate with bio-oil modification for photo-curing 3D printed flexible structures,” *Polymer (Guildf)*, vol. 306, Jun. 2024, doi: 10.1016/j.polymer.2024.127225.

[31] M. In het Panhuis et al., “A COMPOSITE FROM SOY OIL AND CARBON NANOTUBES,” *Int. J. Nanosci.*, vol. 02, no. 03, pp. 185–194, Jun. 2003, doi: 10.1142/s0219581x0300119x.

[32] Sigma-Aldrich, “412333-BULK,” Product Specification. [Online]. Available: www.sigmaaldrich.com.

[33] C. Dietlin et al., “Photopolymerization of Thiol-Alkene Systems: A Review,” *Polymers*, vol. 7, no. 12, pp. 1–20, Dec. 2015, doi: 10.3390/polym7121503.

[34] S. C. Ligon et al., “Polymers for 3D Printing and Customized Additive Manufacturing,” *Chem. Rev.*, vol. 117, no. 15, pp. 10212–10290, Aug. 2017, doi: 10.1021/acs.chemrev.7b00074.

[35] J. Zheng et al., “3D printing of vitrimers: Challenges and opportunities,” *Macromol. Rapid Commun.*, vol. 42, no. 13, p. 2100411, Jul. 2021, doi: 10.1002/marc.202100411.

[36] Sigma-Aldrich, “Product Specification Sheet: Glycerol 1,3-diglycerolate diacrylate (Product Number 475807),” Merck KGaA, 2024. [Online]. Available: https://www.sigmaaldrich.com.

[37] Sigma-Aldrich, “Safety Data Sheet: Ethyl(2,4,6-trimethylbenzoyl)phenylphosphinate (Product Number 726303),” Merck KGaA, 2024. [Online]. Available: https://www.sigmaaldrich.com.

[38] Miwon Specialty Chemical, “Technical Data Sheet: Miramer A99 (Phosphate Methacrylate),” Miwon Specialty Chemical Co., Ltd., 2024. [Online]. Available: http://www.miwon.com.

[39] K. S. Anseth and C. N. Bowman, “A kinetic model of the photopolymerization of dimethacrylates,” *Polymer*, vol. 36, no. 18, pp. 3475–3485, Sep. 1995, doi: 10.1016/0032-3861(95)94781-I.

[40] W. D. Cook, “Photopolymerization kinetics of dimethacrylates using the camphorquinone/amine initiator system,” *Polymer*, vol. 33, no. 3, pp. 600–609, Jan. 1992, doi: 10.1016/0032-3861(92)90738-S.

[41] H. Pelletier, A. Belvedere, N. Vitale, and S. J. Sangermano, “Photopolymerization of bio-based resins: Kinematics and properties of acrylated epoxidized soybean oil,” *European Polymer Journal*, vol. 121, no. 1, p. 109315, Dec. 2019, doi: 10.1016/j.eurpolymj.2019.109315.

[42] M. I. Vonsul, R. Dhandapani, and D. C. Webster, “Moving towards Sustainability: Assessment of Vitrimer Behavior and Reprocessability of Plant Oil-Based Material,” *Polymer*, vol. 317, p. 127941, Jan. 2025, doi: 10.1016/j.polymer.2024.127941.

[43] S. Grauzeliene, A. S. Schuller, C. Delaite, and J. Ostrauskaite, “Biobased Vitrimer Synthesized from 2-Hydroxy-3-Phenoxypropyl Acrylate, Tetrahydrofurfuryl Methacrylate and Acrylated Epoxidized Soybean Oil for Digital Light Processing 3D Printing,” *European Polymer Journal*, vol. 198, p. 112424, Sept. 2023, doi: 10.1016/j.eurpolymj.2023.112424.

[44] T. Liu, S. Zhang, C. Hao, C. Verdi, W. Liu, H. Liu, and J. Zhang, “Glycerol Induced Catalyst-Free Curing of Epoxy and Vitrimer Preparation,” *Macromolecular Rapid Communications*, vol. 40, no. 7, p. 1800889, Apr. 2019, doi: 10.1002/marc.201800889.

[45] M. Zarek, M. Layani, I. Cooperstein, E. Sachyani, D. Cohn, and S. Magdassi, “3D Printing of Shape Memory Polymers for Flexible Electronic Devices,” *Advanced Materials*, vol. 28, no. 22, pp. 4449–4454, Jun. 2016, doi: 10.1002/adma.201504839.

[46] J. Zhao, R. W. J. Scott, and J. C. Bergstrom, “Effect of Resin Viscosity on the Precision of Stereolithography 3D Printing,” *Journal of Manufacturing Processes*, vol. 56, pp. 1020–1028, Aug. 2020, doi: 10.1016/j.jmapro.2020.04.056.

[47] T. Bhattacharjee et al., “Writing in the granular gel medium,” *Science*, vol. 348, no. 6235, pp. 666–669, May 2015, doi: 10.1126/science.aaa1187.

[48] C. Bowman and S. K. Linn, “Review of semi-analytical and numerical models for diffusion-limited radical photopolymerization,” *Polymer*, vol. 45, no. 12, pp. 3981–3994, May 2004, doi: 10.1016/j.polymer.2004.03.040.

[49] J. La Scala and R. P. Wool, “Effect of fatty acid composition on properties of fatty acid-modified thermosetting polymers,” *Journal of Applied Polymer Science*, vol. 91, no. 4, pp. 2433–2443, Feb. 2004, doi: 10.1002/app.13396.

[50] W. Denissen, J. M. Winne, and F. E. Du Prez, “Vitrimers: permanent organic networks with dynamic covalent bonds,” *Chemical Science*, vol. 7, no. 1, pp. 30–38, 2016, doi: 10.1039/C5SC02223A.

[51] K. P. Menard and N. R. Menard, *Dynamic Mechanical Analysis*, 3rd ed. Boca Raton, FL, USA: CRC Press, 2020, doi: 10.1201/9780429190308.

[52] F. I. Altuna, C. E. Hoppe, and R. J. J. Williams, “From soybean oil to recyclable amylopectin-based vitrimers,” *European Polymer Journal*, vol. 82, pp. 100–109, Sep. 2016, doi: 10.1016/j.eurpolymj.2016.07.001.

Ringraziamenti

Ci sono traguardi che non si misurano in pagine o grafici, ma nei passi incerti di chi ha temuto, più volte, di non vederne mai la fine. Questa tesi arriva dopo un cammino lungo, silenzioso, a tratti ripido, dove la meta sembrava sbiadire dietro la stanchezza. Se oggi, però, queste parole trovano una forma compiuta, è perché, anche nei momenti più difficili, non mi sono mai sentito solo.

Desidero ringraziare, innanzitutto, la mia relatrice, la Dott.ssa Camilla Noè, per avermi dato l’opportunità di sviluppare questo lavoro di tesi, per la disponibilità ed il supporto costante, per la pazienza e, soprattutto, per avermi trasmesso l’entusiasmo e quella passione per la ricerca che non credevo di possedere. La tua fiducia è stata fondamentale per ritrovare la mia.

Un grazie sincero a tutto il gruppo “Polymers” del Prof. Massimo Messori, ai dottorandi e ai colleghi tesisti con cui ho condiviso le giornate al “Burner Rig”. Tra attese, test, fallimenti, momenti di confronto e piccole, grandi vittorie, avete reso questa esperienza non solo formativa, ma anche, e soprattutto, umana.

Alle mie “signore”, oramai più che due semplici coinquiline. Grazie per la quotidianità condivisa e per i momenti di leggerezza, per aver saputo abitare con me questo tempo sospeso e per aver reso casa un porto sicuro in cui tornare e ritrovarsi, sempre!

Agli amici di sempre, vicini e “lontani”, quelli che ci sono dalla vita intera e che il tempo ha reso indispensabili. Siete stati il punto fermo in ogni fase di questo percorso. Grazie per aver amplificato ogni mia felicità e per aver reso lievi i momenti più duri. Grazie perché, nonostante le mie assenze e i miei improvvisi “ritiri dal mondo”, siete ancora lì ad aspettarmi. Grazie perché riuscite a capirmi sempre, oltre le parole e oltre le spiegazioni. È nei vostri sguardi che ho riconosciuto il volto della vera amicizia: mi avete insegnato che non importa quanto io possa allontanarmi, perché le radici che ci legano non conoscono tempo né distanza.

Infine, il ringraziamento più profondo va alla mia famiglia. A mio fratello, presenza silenziosa ma preziosa, e ai miei genitori: siete stati l’argine alla mia esondazione, la roccia su cui ho costruito ogni tentativo di ripartenza. Grazie per aver sostenuto i miei silenzi e le mie paure, per avermi dato la forza di continuare, quando io non ne vedevo più, e per aver creduto in me oltre ogni ragionevole dubbio. Questo traguardo appartiene a voi.

Questa non è solo la fine di un percorso accademico, significa molto di più: è la prova che, anche quando tutto sembra fermo, qualcosa dentro continua a muoversi, a resistere, a costruire la strada. E se oggi sono qui, se alla fine ce l’ho fatta, è grazie a tutti voi: a chi ha saputo aspettarmi, sostenermi e, magari senza saperlo, tenermi in cammino.